

Metallomics

Accepted Manuscript



This is an *Accepted Manuscript*, which has been through the Royal Society of Chemistry peer review process and has been accepted for publication.

Accepted Manuscripts are published online shortly after acceptance, before technical editing, formatting and proof reading. Using this free service, authors can make their results available to the community, in citable form, before we publish the edited article. We will replace this *Accepted Manuscript* with the edited and formatted *Advance Article* as soon as it is available.

You can find more information about *Accepted Manuscripts* in the [Information for Authors](#).

Please note that technical editing may introduce minor changes to the text and/or graphics, which may alter content. The journal's standard [Terms & Conditions](#) and the [Ethical guidelines](#) still apply. In no event shall the Royal Society of Chemistry be held responsible for any errors or omissions in this *Accepted Manuscript* or any consequences arising from the use of any information it contains.

1
2
3 1 ***Trace element landscape of resting and activated human***
4 2 ***neutrophils on the sub-micrometer level***
5
6
7

8 4 Niemiec MJ¹, De Samber B², Garrevoet J², Vergucht E², Vekemans B², De Rycke R³,
9 5 Björn E⁴, Sandblad L⁵, Wellenreuther G⁶, Falkenberg, G⁶, Cloetens P⁷, Vincze L² &
10 6 Urban CF¹

11
12 7 ¹ Department of Clinical Microbiology / MIMS, Umeå University, Sweden
13

14 8 ² Department of Analytical Chemistry, Ghent University, Belgium
15

16 9 ³ IRC-PSB Transmission Electron Microscopy-Core Facility, Ghent University,
17 10 Belgium
18

19 11 ⁴ Department of Chemistry, Umeå University, Sweden
20

21 12 ⁵ Department of Molecular Biology, Umeå University, Sweden
22

23 13 ⁶ Petra III, DESY, Hamburg, Germany
24

25 14 ⁷ European Synchrotron Radiation Facility, Grenoble, France
26

27 15
28

29 16
30
31
32
33
34
35
36
37
38
39
40
41
42
43
44
45
46
47
48
49
50
51
52
53
54
55
56
57
58
59
60

1
2
3 174
5 18 **Abstract**

6
7
8 19 Every infection is a battle for trace elements. Neutrophils migrate first to the infection
9 20 site and accumulate quickly to high numbers. They fight pathogens by phagocytosis
10 21 and intracellular toxication. Additionally, neutrophils form neutrophil extracellular traps
11 22 (NETs) to inhibit extracellular microbes. Yet, neutrophil trace element characteristics
12 23 are largely unexplored. We investigated unstimulated and phorbol myristate acetate-
13 24 stimulated neutrophils using synchrotron radiation X-ray fluorescence (SR-XRF) on
14 25 the sub-micron spatial resolution level. PMA activates pinocytosis, cytoskeletal
15 26 rearrangements and the release of NETs, all mechanisms deployed by neutrophils to
16 27 combat infection.

17
18
19
20
21
22
23 28 By analyzing Zn, Fe, Cu, Mn, P, S, and Ca, not only the nucleus but also vesicular
24 29 granules were identifiable in the elemental maps. Inductively Coupled Plasma Mass
25 30 Spectrometry (ICP-MS) revealed a neutrophil-specific composition of Zn, Fe, Cu, and
26 31 Mn in comparison with J774 and HeLa cells, indicating a neutrophil specific
27 32 metallome complying with their designated functions.

28
29
30
31
32 33 When investigating PMA-activated neutrophils, the SR-XRF analysis depicted typical
33 34 subcellular morphological changes: the transformation of nucleus and granules and
34 35 the emergence of void vacuoles. Mature NETs were evenly composed of Fe, P, S,
35 36 and Ca with occasional hot spots containing Zn, Fe, and Ca. An ICP-MS-based
36 37 quantification of NETs supernatants revealed a NETosis-induced decrease of soluble
37 38 Zn, whereas Fe, Cu, and Mn concentrations were only slightly affected.

38
39 39 In summary, we present a combination of SR-XRF and ICP-MS as a powerful tool to
40 40 analyze trace elements in human neutrophils. The approach will be applicable and
41 41 valuable to numerous aspects of nutritional immunity.

42
43
44
45
46 42
47
48
49
50
51
52
53
54
55
56
57
58
59
60

1
2
3 434 44 **Introduction**

5
6
7 45 Metal ions play an important role in many biological processes. They catalyze
8 46 reactions, stabilize structures, and act during gene regulation or cell signaling ¹⁻⁵.
9 47 Their usage is conserved in prokaryotes and eukaryotes ⁶. During infections, when
10 48 the host encounters microbial invaders, metal ions are essential for survival of both
11 49 parties. The host therefore restricts the availability of metal ions in order to avoid
12 50 microbial growth – a strategy named “nutritional immunity” and described in animals
13 51 and plants ⁷. In response, many pathogens have evolved sophisticated tools to
14 52 chelate metal ions from the host and these tools are targeted by the host in return.
15 53 This interplay illustrates co-evolution of host and pathogen and is best exemplified by
16 54 the well-studied fight for Fe ⁸: In the host, Fe is mainly kept intracellular - free Fe is
17 55 essentially unavailable in blood or other extracellular liquids. It is bound to transferrin
18 56 in plasma and lactoferrin in external secretions. Microbial pathogens have two
19 57 mechanisms to cope with these limitations. In case of direct contact between the host
20 58 Fe source and the pathogen, host Fe-retaining proteins are modified to release their
21 59 Fe load into the extracellular environment for uptake. Secondly, many bacteria and
22 60 fungi secrete siderophores, small molecules with exceptionally high Fe affinity that
23 61 free Fe from host proteins followed by resorption into the pathogenic cell. As a
24 62 response, mammals produce lipocalin-2, to intercept siderophores. This can in turn
25 63 be counteracted by many pathogens which disguise their siderophores by
26 64 glycosylation ⁸.

27
28
29
30
31
32
33
34
35
36
37
38
39
40
41 65 Fe is not the only transition metal important in nutritional immunity. Zn, Mn and Cu
42 66 are also shown to be critical ^{9, 10}. Especially Zn has been shown to be crucial during
43 67 fungal pathogenicity ¹¹. This can be explained by its unique biochemical features
44 68 which are reflected in the utilization in different organisms. Zn is a strong Lewis-acid,
45 69 water-soluble at the oxidated state +II and also redox-stable under standard
46 70 physiological conditions ¹². About 7% of the entire proteome of archae, bacteria and
47 71 eukaryotes are predicted to be Zn proteins¹³. In addition to the enzymatic function in
48 72 peptidases, amidases and esterases – conserved to similar extent in all kingdoms –
49 73 Zn functions also in Zn-finger proteins to mediate binding to DNA and RNA. Whereas
50 74 bacteria and archae have less than 0.5% of Zn-finger proteins, eukaryotes have
51 75 about 3% - so almost half of the entity of their Zn proteome ¹³. In agreement with this,
52
53
54
55
56
57
58
59
60

1
2
3
4
5
6
7
8
9
10
11
12
13
14
15
16
17
18
19
20
21
22
23
24
25
26
27
28
29
30
31
32
33
34
35
36
37
38
39
40
41
42
43
44
45
46
47
48
49
50
51
52
53
54
55
56
57
58
59
60

76 fungi are especially susceptible to Zn depletion. Shortage of Zn has been shown to
77 cause intracellular oxidative stress in yeast ¹⁴. Also, the fungal pathogen *Candida*
78 *albicans* was found to be completely growth arrested, if the surrounding
79 concentration of Zn drops below 1 μM ¹⁵.

80 Neutrophils play a crucial role in the immune defense against fungal and bacterial
81 pathogens. Once a pathogen passes the mechanical barrier formed by epithelial cells
82 and penetrates into the underlying tissue, surrounding cells sense the pathogen and
83 send signals that recruit neutrophils to the site of infection. Since neutrophils circulate
84 in a ready-to-use state, influx into tissue can occur fast and exceedingly ¹⁶. Upon
85 contact with invaded microbes, neutrophils fight pathogens in a well-orchestrated
86 sequence of recognition, phagocytosis, intra- and extracellular toxification and local
87 retainment ¹⁷.

88 These functions are all facilitated by the unique morphology of neutrophils. The
89 nucleus is lobulated, allowing the cell to squeeze through layers of tissue. High
90 numbers of granules store antimicrobial peptides and proteins that can be either
91 secreted into the surrounding of the neutrophils or into the phagolysosome ¹⁸. The
92 latter is a highly inhospitable cellular compartment that retains the phagocytosed
93 pathogen. Inside, the pathogen encounters not only antimicrobial peptides and
94 proteins, but also low pH and reactive oxygen and nitrogen species ¹⁹. In addition to
95 secretion and phagocytosis, neutrophils form also extracellular traps (NETs) ²⁰.
96 During NET formation, the nuclear membrane followed by granule membranes and
97 finally the cytoplasmic membrane lose integrity. This allows compartments to mix that
98 are usually separated. NETs consist of DNA, histones, and cytoplasmic and granular
99 proteins ²¹.

100 Calprotectin is one of the NET effector proteins ²². It is the most abundant protein in
101 the neutrophilic cytoplasm, usually not secreted by intact neutrophils, but released
102 during NET formation. Calprotectin is crucial for the NETs efficacy towards bacterial
103 and fungal pathogens, which is due to its Mn and Zn chelating properties ²²⁻²⁵. It has
104 been shown earlier that NET-mediated growth inhibition of *Candida albicans* and
105 *Aspergillus nidulans* could be reversed by the addition of Zn. Whether NET formation,
106 a process of complete cell burst, actually reduces the availability of Zn for the fungal
107 pathogen remains unexplored.

1
2
3 108 On these grounds, we aimed to elucidate the trace elemental properties of human
4 109 neutrophils – resting and activated. To do so, we combined SR micro/nano-XRF,
5 110 ICP-MS, and live cell imaging. The sample preparation for the SR-XRF
6 111 measurements was adjusted to optimize the neutrophil analysis: In order to quantify
7 112 whole neutrophils and analyze filamentous NETs with optimally preserved metal
8 113 contents, entire cells were seeded on a Si₃N₄ wafer and freeze-dried. To investigate
9 114 neutrophils with the highest possible subcellular resolution and analyze intracellular
10 115 metal concentrations, neutrophils were high-pressure frozen (HPF), cryosubstituted
11 116 and sliced in 2 μm thin sections. Using ICP-MS, we quantified neutrophil
12 117 supernatants *post* NET formation and neutrophil full cell lysates for total metal
13 118 content. Lastly, we investigated the distribution of labile Zn in living cells by applying
14 119 the fluorophore FluoZin in activated neutrophils.

15 120 In summary, we successfully analyzed the trace element distributions of human
16 121 neutrophils down to nanoscopic levels using SR-XRF complemented with ICP-MS
17 122 analysis and live cell imaging. While ICP-MS is a broadly used technique, reports of
18 123 SR-XRF for analysis of biological samples are still scarce²⁶⁻²⁸. To our knowledge,
19 124 this is the first study to use SR-XRF at the micro- and nanoscopic level on individual
20 125 innate immune cells. Earlier work included for instance single neurons and
21 126 keratinocytes, but also a variety of other biological sample fluids, tissues and even
22 127 whole small organisms like mussel larvae or the water flea²⁹⁻³⁵. SR-XRF offers
23 128 spatially resolved (down to 50 nm resolution) and quantitative insights (sub-ppm
24 129 level) that can contribute to the in-depth understanding of the site of infection as a
25 130 nutritional niche. The approach presented will be applicable and valuable to
26 131 numerous aspects of nutritional immunity.

27 132

28 133

134

135 Results

136 *Trace-level metallome of human neutrophils determined by SR-XRF and ICP-* 137 *MS*

138 High influx of neutrophils to the site of infection very likely affects the local metal
139 environment. In this context, transition metals are particularly important for nutritional
140 immunity. We measured the neutrophil suspension diameter as $8.85 \pm 0.44 \mu\text{m}$ and
141 using this value calculated the total cellular concentration of metal ions assuming an
142 even spherical shape of the cells, resulting in a cell volume of approx. $363 \mu\text{m}^3$. We
143 used ICP-MS to analyze the neutrophil's total content of Zn, Fe, Cu, and Mn.
144 Neutrophil lysates from 10^7 cells per sample were conducted to ICP-MS, resulting in
145 the following metallome: freshly isolated human neutrophils were found to contain
146 $6.07 \pm 1.29 \times 10^7$ Zn atoms, $1.64 \pm 0.33 \times 10^8$ Fe atoms, $2.26 \pm 0.69 \times 10^6$ Cu atoms,
147 and $2.49 \pm 0.69 \times 10^5$ Mn atoms (Tab. 1). The total cellular concentration was
148 calculated similarly: $[\text{Zn}] = 275.31 \pm 58.61 \mu\text{M}$, $[\text{Fe}] = 743.91 \pm 148.62 \mu\text{M}$, $[\text{Cu}] =$
149 $10.24 \pm 3.11 \mu\text{M}$, and $[\text{Mn}] = 1.13 \pm 0.31 \mu\text{M}$ (Tab. 1). To obtain information on the
150 spatial distribution of trace-level metals within neutrophils we scanned whole cells
151 using micro/nanobeam SR-XRF, fitted the individual point spectra and generated the
152 elemental maps. In addition to the information on spatial distribution, XRF was used
153 to quantitatively determine the neutrophil metallome using an ICP-MS-independent
154 method. The total XRF spectrum of a single neutrophil was obtained by region-of-
155 interest selection and summing up the individual XRF spectra belonging to the single
156 cell, followed by quantification of the cell sum spectrum using a glass trace-element
157 calibration standard. Based on the measurements of three individual freeze-dried
158 neutrophils, an average neutrophil was determined to contain $6.94 \pm 0.86 \times 10^7$ Zn
159 atoms, $9.38 \pm 1.11 \times 10^6$ Fe atoms, $1.38 \pm 0.18 \times 10^7$ Cu atoms, and $8.73 \pm 1.76 \times$
160 10^5 Mn atoms (Tab. S1). Accordingly, the total cellular concentrations were
161 calculated: $[\text{Zn}] = 317.35 \pm 39.17 \mu\text{M}$, $[\text{Fe}] = 42.91 \pm 5.09 \mu\text{M}$, $[\text{Cu}] = 63.27 \pm 8.17 \mu\text{M}$,
162 and $[\text{Mn}] = 3.99 \pm 0.80 \mu\text{M}$ (Tab. S1). In comparison, the two different techniques
163 resulted in partially different neutrophil metallomes. The determined concentration of
164 cellular Zn was consistent between the two techniques. Zn is known to have total
165 cellular concentrations of 0.1-0.5 mM, so both neutrophil concentrations determined
166 are also well in range with other mammalian cells¹². SR-XRF determined total metal

1
2
3 167 contents were approximately 3 and 6-fold higher than ICP-MS for Mn and Cu,
4 168 respectively. Finally, the cellular Fe level ICP-MS quantification resulted in an
5 169 approximately 17-fold higher value than XRF. From this point on, we use and refer to
6 170 the ICP-MS metallome, due to a higher statistical certainty – we used 8 different
7 171 donors and 10^7 cells per sample.

8 172 To test the hypothesis that neutrophils might be purposely low in metal ions to
9 173 compensate for their high influx to infection sites, we included two other mammalian
10 174 cells frequently used in molecular infection research: macrophage-like J774 cells and
11 175 HeLa cells. Since both cells are larger than neutrophils, we were not surprised to find
12 176 a higher total metal content for J774 and HeLa cells. In suspension, J774 cells have
13 177 a diameter of 15.8 μm ; HeLa cells have a diameter of 22 μm ^{36, 37}. Accordingly, the
14 178 volumes of these cells differ greatly. The calculated volumes were 363 μm^3 , 2065
15 179 μm^3 , and 5575 μm^3 for neutrophils, J774 and HeLa cells, respectively. When the
16 180 metal content was normalized to cell volume, we found J774 cells to be slightly richer
17 181 in Zn and Cu, much richer in Mn, and poorer in Fe. HeLa cells had a similar Zn and
18 182 Cu density, slightly increased Mn content, and a lower level of Fe as well (Fig. 1).
19 183 This data indicates that neutrophils are higher in Fe than the other two cell types
20 184 analyzed.

21 185

22 186 ***Distribution of P, S, Ca, Zn, Fe, Cu, and Mn in human resting neutrophils***
23 187 ***(obtained at P06 beamline, PETRA III)***

24 188 SR-XRF measurements were performed at the P06 Hard X-ray Microprobe (PETRA
25 189 III, Hamburg, Germany) providing at the time of the measurement a beam size of 0.5
26 190 μm (vert.) x 0.4 μm (hor.) FWHM. The scanning step size was typically 1 μm
27 191 (compromise between covering a large area for NET visualization and sufficient
28 192 resolution). Freshly isolated neutrophils were seeded onto Si_3N_4 wafers, plunge-
29 193 frozen in liquid ethane, and finally freeze-dried. Freeze-drying of whole cells was
30 194 chosen to preserve elemental integrity - at the expense of morphology collapse³³;
31 195 entire cells were analyzed in this 'whole-cell' set-up. Neutrophils of interest were
32 196 selected based on their light-microscopic appearance and then analyzed by SR-XRF
33 197 – representative images are discussed in the following (Fig. 2A). Strikingly, the most
34 198 prominent feature of neutrophils - the lobulated nucleus – stood out against the
35 199 cytoplasm by an increased signal from P and Zn. The cytoplasm displayed areal
36 200 concentrations above background level for the elements P, S, Zn, and Fe. Several

1
2
3 201 potential contaminations were found, one of them in close proximity to the nucleus,
4 202 slightly overlaying the neutrophil. In this and in randomly distributed 'speckles' on the
5 203 entire sample, we detected P, S, Ca, and Fe. To complement our observations, we
6 204 aimed to quantify the trace element content of nucleus and cytoplasm. Since surface-
7 205 attached neutrophils vary in thickness and total mass per area was not determined,
8 206 average concentrations of metals in nucleus and cytoplasm could only be determined
9 207 in approximation (Tab. S2). We found a higher average areal concentration of Zn and
10 208 Fe in the nucleus as compared to the cytoplasm. Cu had a very low, but almost equal
11 209 areal concentration in nucleus and cytoplasm (with the nucleus being thicker), while
12 210 Mn was found to show higher areal concentrations in the cytoplasm.
13
14
15
16
17
18
19
20

211

212 ***Distribution of P, S, Ca, Zn, Fe, Cu, and Mn in activated human neutrophils and***
213 ***NETs (obtained at P06 beamline, PETRA III)***

214 Similarly to the previous section ('whole-cell' set-up), freshly isolated neutrophils were
215 seeded directly onto Si₃N₄ wafers and stimulated with phorbol-myristate acetate
216 (PMA) to induce ROS production, internalization events and NET formation. After 2 h
217 and 4 h, the samples were plunge-frozen and freeze-dried to preserve morphology.
218 Unstimulated neutrophils were also included (see previous section). A 4 h stimulation
219 with PMA is sufficient to cause a nearly full conversion of neutrophils to NETs^{21, 38}.
220 The 2 h stimulation represents an intermediate stage (Fig. 2B). As mentioned, the
221 analysis of unstimulated neutrophils revealed clear differences between the nucleus
222 and the cytoplasm. After 2 h stimulation, the morphology of the neutrophils changed
223 considerably, but not in a perfectly synchronized fashion. Some neutrophils engaged
224 in the process of NET formation earlier than others. The progress of NET formation is
225 most apparent when following the nucleus. In early NET formation, the nucleus loses
226 its lobulation and shrinks to form a smaller and round shape (Supplement, S3, * + a).
227 The lower neutrophil #1 is representative of this stage (Fig. 2B). As in unstimulated
228 neutrophils, the nucleus contained a higher areal concentration of P and Zn, whereas
229 the cytoplasm featured a homogeneous distribution of P and S (higher areal
230 concentration than background level). Interestingly, the intact stimulated neutrophil
231 also showed the presence of an Fe rich region, distributed in a ring-like manner in the
232 cell periphery. The upper neutrophil #2 is representative of a later stage of NET
233 formation, characterized by the loss of membrane integrity, first of the nucleus, then
234 of the cytoplasmic membrane – the cell opens up and lyses (Supplement, S3, b + c).

21
22
23
24
25
26
27
28
29
30
31
32
33
34
35
36
37
38
39
40
41
42
43
44
45
46
47
48
49
50
51
52
53
54
55
56
57
58
59
60

1
2
3 235 When comparing the light microscope images of neutrophil #2 with neutrophil #1, we
4 236 observe that from the area initially covered by neutrophil #1, only cell residues in
5 237 neutrophil #2 remain visible. The SR-XRF elemental maps confirm that the upper cell
6 238 has likely lysed: within the area of the cell (shape of an inverted heart or leaf), we
7 239 could no longer observe the homogeneous distribution of P and S. In contrast, the
8 240 remaining cell debris was enriched in P, S, Ca, Fe, and Zn. A hotspot containing not
9 241 only these elements, but also Cu and Mn was found to be within the area of
10 242 neutrophil #2. This is most likely a non-biological contamination. Short fiber-like
11 243 structures, which we identified as NETs, are protruding out of the cell debris. Areal
12 244 concentrations for P, S, Zn, and Fe were found to be above background level. Similar
13 245 to the unstimulated sample, several 'hot-spots' (1-4 μm size) containing P, S and Ca
14 246 are present which could be cell remnants. After 4 h of stimulation, NET formation was
15 247 completed and no intact neutrophils were remaining (Fig. 2C). The typical orbital
16 248 patches of cellular debris were as prominent as long filamentous fibers of NETs with
17 249 a thickness at least below 1 μm (estimation of size was limited by the step size of the
18 250 scanning stages). The SR-XRF analysis clearly showed the NETs structure in the
19 251 elemental maps of P, S, Ca and Fe. No strong accumulation of Zn could be detected
20 252 in NETs, which is remarkable considering the high intracellular content of Zn in the
21 253 neutrophil. This indicates that freshly releases NETs, under the given cell culture
22 254 conditions with very low medium concentrations of Zn, are not loaded with Zn, yet. As
23 255 mentioned, we observed high local Ca and Fe concentrations in NETs which were
24 256 not detected within intact neutrophils. This finding correlates well with rather high
25 257 concentrations of Ca (400 μM Ca, according to manufacturer's information) and Fe
26 258 (0.7 μM according to ICP-MS quantification, data not shown) in the surrounding
27 259 medium. Several Ca, Fe and Zn rich spots having varying XRF intensity were
28 260 detected in the vicinity of the NET structures. Consulting the microscopy images,
29 261 these could be contaminations, cell debris or uneven twisting of numerous NETs from
30 262 numerous neutrophils. In summary, SR-XRF scans providing elemental distributions
31 263 reconstitute the typical architecture of neutrophils at the microscopic level and
32 264 allowed discrimination of nucleus, cytoplasm and far-reaching (up to 100 μm) NETs.
33 265 Strikingly, cellular morphology changes accompanying NET formation and even NET
34 266 filaments were visible in the element maps.
35 267

1
2
3 268 ***Trace level metal distribution of nucleus and cytoplasm in resting neutrophils***
4 ***(obtained at ID22NI beamline, ESRF)***
5

6 270 For the analysis of human neutrophils at the ID22NI (nano-imaging) beamline
7
8 271 (European Synchrotron Radiation Facility (ESRF), Grenoble, France), cells were
9
10 272 seeded onto sapphire disks, conducted to high pressure freezing (HPF) and cryo-
11
12 273 substituted into resin before being sliced into 2 μm thin sections. We will refer to this
13
14 274 as the 'sectioned' approach. In order to slice neutrophils at this scale, fixation and
15
16 275 embedding were inevitable ³¹. We minimized the procedure's impact on element
17
18 276 integrity by including wash steps and reducing exposure time to potential
19
20 277 contamination sources. The beam size was estimated to be 64 nm (vert.) by 54 nm
21
22 278 (hor.) and the step size of the scans was 50 nm. Images of representative cells are
23
24 279 discussed in the following.

25
26 280 As observed before, the neutrophil nucleus stood out due to its distinct increase in
27
28 281 metal content relative to the cytoplasm. Remarkably, the higher resolution revealed
29
30 282 more subcellular detail than observed in the previous analysis (Fig. 3A). As a
31
32 283 morphology reference, we used corresponding sections from the same sample
33
34 284 imaged with transmission electron microscopy. The typical lobulated nucleus of an
35
36 285 unstimulated neutrophil was distinguishable by increased areal concentrations of P,
37
38 286 Ca, Zn, Fe, and Mn. These elements were not evenly distributed within the nucleus,
39
40 287 but seemed to be more abundant in the outer region, closer to the nuclear
41
42 288 membrane. The pattern is reminiscent of hetero- and euchromatin. Additionally, the
43
44 289 Fe distribution showed round patches with increased Fe intensity, which might be
45
46 290 nucleoli, the largest structures within the nucleus. Interestingly, S and Cu displayed
47
48 291 an inverted pattern compared to the other elements: lowest intensity in peripheral
49
50 292 regions of the nucleus and presence in higher amounts within inner regions and cell
51
52 293 cytoplasm. As we find both elements also in the surrounding matrix material, their
53
54 294 presence in the cytoplasm must be considered very cautiously. Then again, a higher
55
56 295 concentration of S in the cytoplasm is consistent with the high prevalence of
57
58 296 reducing, S-containing, molecules and proteins in the cytosol ³⁹. The presence of Cu
59
60 297 in the neutrophil cytoplasm appears likely, as Cu is an essential trace element ⁴. In
298 the periphery of the cells (at the edges of the scans), we observed a halo-like area of
299 higher S and Cu concentration. This halo in the S and Cu maps very likely originates
300 from S and Cu presence in the embedding resin. In areas with low biological mass,
301 the beam-induced warm up of the samples probably caused the resin to shrink, and

1
2
3 302 therefore locally increased the concentration of elements in the resin. In the
4 303 cytoplasm, Ca was homogeneously present, whereas Fe and Zn showed a speckled
5 304 pattern, most probably resulting from neutrophil-characteristic granules loaded with
6 305 antimicrobial proteins. The speckles had an average size of 200 nm, which matches
7 306 earlier studies that have shown granule size varying between 0.14 μm and 0.29 μm
8 307 ⁴⁰. The Zn speckles were generally smaller in size than those formed by Fe. An
9 308 overlay of the Zn and Fe elemental maps revealed that the granular speckles did not
10 309 always co-localize, which indicates the presence of a variety of granules. For our
11 310 comparative analysis of nucleus and cytoplasm (Tab. 2), the speckles (potentially
12 311 granular) or subnuclear structures were too small to be excluded from the cytoplasm.
13 312 Since 2 μm thin sections of single neutrophils were analyzed, the integration of the
14 313 total illuminated mass signal of the entire cell depth along the beam path can be
15 314 ruled out. Average areal concentrations of P, S, Ca, Zn, Fe, Cu, and Mn confirm our
16 315 previous observation that most elements were preferentially enriched in nucleus or
17 316 cytoplasm – only Fe seemed to be almost evenly distributed. In order to obtain
18 317 quantitative insight in the inhomogeneous presence of metals in the nucleus as
19 318 compared to the cytoplasm, we calculated a so-called ‘enrichment factor’: P (50.11 x)
20 319 > Zn (3.19 x) > Ca (2.83 x) > Mn (3.98 x) > Fe (1.29 x). For the less abundant
21 320 elements we found: S (0.47 x) < Cu (0.63 x). In summary, these data indicate higher
22 321 concentrations of P, Zn, Ca, and Mn, as well as lower concentrations of S and Cu in
23 322 the nucleus as compared to the cytoplasm.

24
25
26
27
28
29
30
31
32
33
34
35
36
37
38 323 Clearly, the measurements at ID22NI allowed the detection and spatial analysis with
39 324 higher sensitivity than SR-XRF measurements at PETRAIII. The major differences
40 325 between the two experiments and results in spatial distribution are mentioned in the
41 326 text where appropriate and were additionally summarized in a comparing table (Tab.
42 327 S4).

43
44
45
46 328

47
48 329 ***Nanoscale elemental distributions of P, S, Ca, Zn, Fe, Cu, and Mn in activated***
49 330 ***human neutrophils (obtained at ID22NI beamline, ESRF)***

50
51 331 Similar to unstimulated cell preparations, cells were seeded on sapphire disks and,
52 332 apart from PMA stimulation, prepared identically. However, more time points were
53 333 included in order to relate cellular changes during activation and NET formation with
54 334 differences in metal distribution.
55
56
57
58
59
60

1
2
3 335 Neutrophils activated for 1 h showed similar metal distributions of P, S, Ca, Zn, Fe,
4 336 Cu and Mn resulting in similar visibility of nucleus and cytoplasm (Fig. 3B). Fe
5 337 speckles were again rougher and more dominant than Zn speckles present in the
6 338 cytoplasm, and likewise low concentration of Ca could be detected in the cytoplasm.
7
8 339 Interestingly, the cytoplasm of these briefly stimulated neutrophils revealed void
9 340 vacuoles with visibly reduced concentrations of Ca, Fe, Zn, and Cu. Neutrophils are
10 341 known to generate cytoplasmic membrane vacuoles upon strong stimulation. These
11 342 vacuoles are formed by the internalization of extracellular liquid (pinocytosis) and
12 343 show similarities to phagosomes⁴¹. Thus, the low metal content in voids of PMA-
13 344 stimulated neutrophils are consistent with the metal composition of phagosomes,
14 345 membrane-surrounded compartments which contain engulfed microbes and are also
15 346 known to be low in Zn, Fe, and Mn⁷. At 2 h and 3 h *post stimulation*, the morphology
16 347 of the nucleus as well as its inner elemental distribution was altered tremendously
17 348 (Fig. 3C + 3D). The lobulated shape of the nucleus disappeared and yet, enrichment
18 349 of Ca, Mn, and Zn (and P) was still observed. The distribution of those elements
19 350 within the nucleus however, was more homogenous than in nuclei from resting cells.
20 351 This indicates that nuclei might have remained intact to this point, whereas
21 352 separation of inner and outer nuclear region was lost. The cytoplasmic membrane,
22 353 depicted by the Zn element map in resting cells, disappeared at these later stages.
23 354 Even after a stimulation of 3 h, void vacuoles characterized by the strongly reduced
24 355 intensity of Zn and Fe were still present, at these stages in close proximity to the
25 356 nuclei and smaller than during earlier stages. Finally, after 4 h of stimulation, it was
26 357 increasingly difficult to locate nuclei or whole cells (Fig. S5). The intensities in all
27 358 elemental maps were close to the background level probably caused by the cell burst
28 359 spreading the intracellular content over a larger volume and therefore decreasing the
29 360 areal elemental concentration. In summary, synchrotron XRF analysis with a spatial
30 361 resolution at the 50 nm level revealed the elemental composition of neutrophil
31 362 nucleus and cytoplasm and enabled detection of nuclear structures as well as
32 363 cytoplasmic granules based on distinct element signals.
33
34
35
36
37
38
39
40
41
42
43
44
45
46
47
48
49
50
51
52

365 **Sample radiation damage and detection of NETs using SR-XRF**

366 We believe that the conditions for observing NETs in the high resolution (ID22NI)
367 elemental maps starting from 2 h *post activation* are particularly challenging due to
368 the following reasons. First of all, later stages of NET formation are accompanied by
369
370
371
372
373
374
375
376
377
378
379
380

1
2
3 369 the loss of cell integrity, resulting in decreased areal concentrations of metals,
4 370 resulting in higher signal-to-noise ratio. A second reason is the more pronounced
5 371 sample radiation damage due to photo and auger electrons, depositing their energy
6 372 locally. In Fig. 3D and S5, the sample radiation damage occurring in the embedding
7 373 resin was surprisingly observed as a flame-like pattern, especially in the Cu map, of
8 374 neutrophils stimulated for 3 h and 4 h. Third, as the sections used in this experiment
9 375 were only 2 μm thick, NETs are sectioned in a random plane and therefore easily
10 376 overlooked by 2D nano-XRF analysis, as their diameter would only encompass a few
11 377 pixels, randomly located within the elemental map. Fourth, the scanning area of
12 378 interest was defined by light microscopy, which is slightly biased in favor of visible
13 379 and integer looking cells.

14
15
16 380 In contrast, conditions for observing NETs in the freeze-dried samples (beamline
17 381 P06, PETRA III) scanned with 1 μm step size were more favourable due to the
18 382 following differences and changes: First, freeze-dried cells are denser than
19 383 embedded cells resulting in less deposited energy and sample radiation damage.
20 384 Second, deposition of the entire three-dimensional cell structure onto a two-
21 385 dimensional wafer gathered all available NETs. And finally, the 'whole-cell' set-up
22 386 increased the areal elemental concentrations of the sample allowing the beam to
23 387 excite elements over the entire depth of the sample. Disadvantages are however the
24 388 lower preservation of the ultrastructure and difficulties in comparing areal
25 389 concentrations (Tab. S4).

26
27
28 390 In general, we can conclude that the combination of the two sample preparation
29 391 approaches: 'whole cell' (freeze-dried whole cells analyzed at the microscale) and
30 392 'sectioned' (shock-frozen, embedded and sectioned cells) were crucial to meet the
31 393 very different needs of resting and activated neutrophils and NETs.
32
33
34
35
36
37

38 394

39 395 ***Presence of Co, Ni, Sr, and Pb in human neutrophils***

40 396 It is a major advantage of SR-XRF compared to ICP-MS that it is unbiased regarding
41 397 the investigated elements – no standard of individual elements is required prior to
42 398 quantification. In agreement with this notion, we detected the elements Co, Ni, Pb
43 399 and Sr which are less-well established as biologically relevant components (Fig. S5).
44 400 Co, Ni, and Pb were accumulated in the nucleus and showed a distribution pattern
45 401 similar to Ca. In contrast, the concentration of Sr was only above background level
46 402 near the cytoplasm border. While the presence of Sr in biological samples is

1
2
3 403 expected - due to its chemical equivalence with Ca and accumulation in bone tissue
4 404 – the presence and distribution of the other elements was less anticipated.
5
6 405 Secondary effects in X-ray fluorescence can often be a source for misinterpretation of
7
8 406 results. In our case, a sudden increase in areal density of the sample (e.g. due to a
9
10 407 more dense nucleus) could have caused a local increase in scattered photons, which
11
12 408 may in turn generate additional fluorescence from the sample environment,
13
14 409 potentially resulting in an increased signal above the expected value. However, we
15
16 410 found little or no variation in the Compton scattering map, indicating that the areal
17
18 411 mass throughout scanned area around the neutrophil is nearly constant. Therefore,
19
20 412 even with a much higher presence of trace level metals in the nucleus, secondary
21
22 413 effects erroneously enhancing the detection of these metals can be excluded in our
23
24 414 case.
25
26 415

416 ***Effects of NET formation on the availability of Zn, Fe, Cu, and Mn***

417 NETs inhibit growth of and kill microbes. The NET-mediated growth inhibition of the
418 fungus *Candida albicans* can be overcome by the addition of Zn^{2+} to the medium²². It
419 is known that NETs contain calprotectin that chelates Zn^{42} . To verify whether NET
420 formation indeed decreases the availability of Zn, even though the entire cell opens
421 up during this process, we analyzed the liquid and protein-filtered supernatant of
422 NETs. Freshly isolated neutrophils were stimulated with PMA for 4 h in the presence
423 of increasing Zn^{2+} concentrations up to 33 μM and the Zn^{2+} concentration of the
424 medium was quantified with ICP-MS before and after NET formation (Fig. 4). We
425 found the remaining Zn^{2+} concentration to be depending on the initial Zn^{2+}
426 concentration, following a saturation curve. With low initial Zn^{2+} concentrations up to
427 ca. 6 μM , the resulting Zn concentration was in the range of 0-51 % of the initial
428 concentration. At initial concentration beyond this, the resulting concentration
429 reached a maximum of approximately 63 % (Fig. 4). We conclude that NET formation
430 indeed reduces the availability of Zn and that there is specific binding at low to
431 medium (< 3-6 μM) and unspecific association at high Zn concentrations (>6 μM). We
432 additionally measured Fe, Cu, and Mn concentrations before and after NET formation
433 and detected only slight reductions of 9 %, 5 %, and 7 %, respectively (Tab. S7).

434

435 ***FluoZin-labeling of labile Zn pool during neutrophil activation***

1
2
3
4
5
6
7
8
9
10
11
12
13
14
15
16
17
18
19
20
21
22
23
24
25
26
27
28
29
30
31
32
33
34
35
36
37
38
39
40
41
42
43
44
45
46
47
48
49
50
51
52
53
54
55
56
57
58
59
60

1
2
3 436 The analysis of activated neutrophils using SR-XRF under routine conditions (i.e.
4 437 without combining it with e.g. X-ray absorption spectroscopic techniques,
5 438 XANES/EXAFS) is only providing element information. Therefore, distinguishing
6
7 439 between strongly and loosely bound Zn is not possible. Strongly bound Zn exists in
8 440 proteins of the Zn proteome, e.g. superoxide dismutase and ribosomes. Loosely
9 441 bound Zn, also called labile or “free” Zn, is associated with all kinds of negatively
10 442 charged molecules like DNA, organic acids or glutathione ¹². An earlier study
11 443 analyzing the distribution of “soluble” and “particulated” Zn in fractions of HepG2 cells
12 444 found 65 % of the Zn to be soluble and 35 % to be in the pellet of a high-speed
13 445 centrifuged cell extract ⁴³. FluoZin can detect the labile Zn pool in living cells and was
14 446 therefore used to complement our findings about the Zn distribution in neutrophils
15 447 during activation of neutrophils and NET release ⁴⁴. FluoZin-stained neutrophils were
16 448 stimulated with PMA and followed by fluorescence-based live cell imaging over ca. 3
17 449 h (video V1). Four observations were most striking: First, the nucleus did not show a
18 450 stronger fluorescence signal compared to the cytoplasm, indicating that the labile Zn
19 451 is not higher concentrated in this organelle. Comparing this with the higher total areal
20 452 Zn concentration in the nucleus observed with SR-XRF, we can deduce that most of
21 453 the Zn is strongly bound and present in the nucleus. Second, void vacuoles with low
22 454 metal content, which were indicated by SR-XRF, were also visualized by FluoZin-
23 455 labeling, confirming the low Zn content of these membrane-surrounded vesicles.
24 456 Third, small round organelles high in labile Zn exclusively appeared after stimulation.
25 457 We cannot distinguish at this point what type of intracellular vesicles these are. They
26 458 also partially remained in the typical cell residues left after full NETosis and could
27 459 therefore additionally contribute to the reduced Zn level after NET formation (Fig. 4).
28 460 Lastly, major reshaping of the intracellular architecture occurred when the cells
29 461 opened up just before NET release. Once this happened, the evenly distributed
30 462 intracellular labile Zn disappeared, probably because Zn was diluted into the low-Zn
31 463 medium. As expected, NETs were not visible in this setting. The cell culture medium
32 464 used contained very low amounts of Zn to avoid background fluorescence, and NETs
33 465 were probably not saturated with Zn under these conditions. Similar effects were also
34 466 seen with strongly bound Zn in the SR-XRF images from PETRAIII (Fig. 2B + 2C).
35 467 Altogether, by FluoZin-labeling we were able to follow the major morphological
36 468 changes in activated neutrophils up to final NET release visualizing the labile Zn pool.
37 469 In contrast to SR-XRF, where Zn showed a higher total Zn areal concentration in the
38
39
40
41
42
43
44
45
46
47
48
49
50
51
52
53
54
55
56
57
58
59
60

1
2
3 470 nucleus, FluoZin-imaging of free Zn indicates a homogenous distribution of the labile
4 471 Zn pool in nucleus and cytoplasm.
5
6

7 472

8 473 **Discussion**

9
10 474 Neutrophils patrol in circulation until they quickly invade a site of infection in high
11 475 numbers and fulfill their antimicrobial task until they reach cell death. The neutrophil
12 476 life time is limited, since their weaponry is too dangerous for the host's own tissue to
13 477 be stored for too long. Apoptosis and NETosis are two important cellular death
14 478 mechanisms of neutrophils. During NETosis, the entire neutrophil opens up to
15 479 release its intracellular content. During apoptosis, the cell stays surrounded by an
16 480 intact membrane and is eventually removed by efferocytosis. A high influx of
17 481 neutrophils into the infectious site, where individual neutrophils end their life by either
18 482 NETosis or apoptosis, serves to remove the threat of invading microbes on the one
19 483 hand, but probably also delivers a sudden nutritional enrichment of the infection
20 484 niche. On these grounds, we performed an in-depth analysis of the trace element
21 485 landscape of human neutrophils. By applying SR-XRF for the first time on single
22 486 neutrophils, we obtained trace element distributions in resting and activated
23 487 neutrophils undergoing pinocytotic events, cytoskeletal rearrangements and NETosis.
24 488 We were able to detect intracellular structures at the size of cytoplasmic granules (\approx
25 489 200 nm) and thin filamentous NETs (below 1 μm diameter, up to 100 μm length). We
26 490 identified the lobulated nucleus and subnuclear structures, compared element
27 491 distributions of nucleus and cytoplasm and followed neutrophil activation in a time
28 492 course until ultimately NETs were released. We quantified the total content of
29 493 biologically relevant metals (Zn, Fe, Cu, Mn) of neutrophil lysates by ICP-MS and
30 494 compared the resulting metallome with intact neutrophils analyzed by SR-XRF. The
31 495 neutrophil metallome was further compared to macrophage-like J774 cells and HeLa
32 496 cells revealing a cell type-specific composition of Zn, Fe, Cu, and Mn with an
33 497 exceptionally high Fe content. In addition, we experimentally demonstrated a specific
34 498 reduction in available Zn by the process of NETosis. Finally, we visualized 1) the
35 499 homogeneously distributed labile Zn pool in activated neutrophils by FluoZin (implying
36 500 a nucleus mainly containing strongly bound Zn resulting from the high Zn areal
37 501 concentration maps in SR-XRF, and 2) the presence of 'void' vacuoles - low in metal
38 502 content - using FluoZin and SR-XRF in living and fixed cells respectively. Void
39
40
41
42
43
44
45
46
47
48
49
50
51
52
53
54
55
56
57
58
59
60

1
2
3 503 vacuoles share features with the early phagosome, since they are also derived from
4 504 pinocytosis, the uptake of extracellular liquids^{7,41}.
5
6 505 Our metallome analysis of neutrophils in comparison to other mammalian cells
7
8 506 commonly used in *in vitro* infection studies indicated a high Fe content in this cell
9
10 507 type. This is also reflected by the ratios of the respective metals. For HeLa cells,
11 508 were determined the following ratios: Zn/Fe 2.0, Zn/Cu 16.7, and Fe/Cu 8.3. For
12 509 macrophage-like J774 cells, the ratios were notably different: Zn/Fe 1.8, Zn/Cu 40.2
13 510 and Fe/Cu 21.9. The ratios of metals in neutrophils were even more distinct: Zn/Fe
14 511 0.4, Fe/Cu 72.6, and Zn/Cu 26.9. Earlier quantifications of 7 different cell culture lines
15
16 512 by total reflection XRF (T-XRF) demonstrated that the ratio of cell metals can differ
17 513 from cell line to cell line, resulting in a range of ratios⁴³. The cell lines investigated
18 514 originated from different tissues and mammals. Primary immune cells were not
19 515 included. Tapia *et al.* compared the concentration of Fe, Cu, and Zn in pelleted cells
20 516 normalized to the protein mass and determined the range of metal ratios to describe
21 517 the metal composition: Zn/Fe 1.4-2.4, Zn/Cu 5.5-21.1, and finally Fe/Cu 3.0-12-3. Mn
22 518 was not considered in this study. A comparison to these findings confirms that
23 519 neutrophils are very high in iron and rather low in Cu. Macrophage-like J774 cells are
24 520 low in Cu, and according to our data richer in Mn than neutrophils. HeLa cells are
25 521 closest to the types of cells analyzed by Tapia *et al.* – and their metal ratios are
26 522 indeed completely in agreement with the ratios described. A possible explanation for
27 523 the very high Fe content of human neutrophils is the high abundance of the enzyme
28 524 myeloperoxidase (MPO), up to 5 % of the cell mass⁴⁵. It contains a heme cofactor
29 525 and produces hypochlorous acid during the oxidative burst. Additionally, neutrophils
30 526 and also macrophages contain the heme-containing enzyme catalase that is used to
31 527 protect against oxidative damage. Lastly, the relative low Mn content of neutrophils
32 528 could result from the low number of mitochondria in these cells⁴⁶. All together, these
33 529 values demonstrate nicely that the metal content of neutrophils is cell type specific.
34 530 Our SR-XRF analysis revealed that typical morphological features of neutrophils are
35 531 also reflected in the spatial distribution of elements. The most striking features of
36 532 resting neutrophils were the lobulated nucleus and speckles that we identified as
37 533 granules. Those granules were enriched in Fe and Zn, and the signal from both
38 534 elements did not overlap completely. Indeed, neutrophils contain a number of
39 535 different granules with partially distinct and partially overlapping content¹⁸.
40
41 536 Interestingly, the enzyme myeloperoxidase (MPO) is exclusively present in so-called
42
43
44
45
46
47
48
49
50
51
52
53
54
55
56
57
58
59
60

1
2
3 537 azurophil granules and contains a heme cofactor ⁴⁵, while neutrophil matrix
4 538 metalloproteases are present in so-called specific granules, and both MMP8
5 539 (collagenase) and MMP9 (gelatinase B) are Zn-dependent. Iron-binding lactoferrin is
6
7 540 also found in specific granules, but since lactoferrin is secreted to sequester iron, it is
8
9 541 unlikely already loaded with Fe in the granules ⁸.

10
11 542 In NETs on the other hand, lactoferrin is exposed to the extracellular environment. It
12
13 543 is therefore likely that lactoferrin bound to NETs can chelate some Fe from the
14
15 544 surrounding. In our study, we found that the Fe concentration in the supernatant of
16
17 545 NETs was slightly decreased and we observed that NETs were enriched in Ca and
18
19 546 Fe. The high content of Fe in NETs is probably originating not only from lactoferrin,
20
21 547 but also from the heme-containing enzymes MPO and catalase, as they are also
22
23 548 known to be bound to NETs ^{22, 47}. Calprotectin is part of the NETome as well. This
24
25 549 protein can bind Ca, and on another binding site Zn and Mn ⁴². It is most likely
26
27 550 responsible for the reduction of available Zn in the supernatant of NETs. Zn chelation
28
29 551 of NETs is important towards fungal pathogens. This is illustrated by the inability of
30
31 552 other metal ions than Zn²⁺ to rescue *Aspergillus nidulans* ²³ and *Candida albicans*
32
33 553 (data not shown) from NET-mediated growth inhibition

34
35 554 These findings shape the view on the nutritional immunological importance of
36
37 555 neutrophils: Compared to other cells, the neutrophil is exceptionally high in Fe. This
38
39 556 is likely the result of a high MPO content in neutrophil granules, which matches our
40
41 557 findings of Fe speckles in the cytoplasm of neutrophils. Other metal-containing
42
43 558 enzymes in neutrophil granules are Zn-dependent metalloproteases. While these
44
45 559 enzymes are released by activated neutrophils, we did not find an increased Fe or Zn
46
47 560 concentration in the supernatant of activated neutrophils. On the contrary, we found
48
49 561 the Zn concentration to be reduced and the Fe concentration to be almost
50
51 562 unaffected. The analysis of NETs confirmed their capacity to bind Zn. Further, void
52
53 563 vacuoles were found in activated neutrophils that were low in Fe and Zn. Void
54
55 564 vacuoles are likely similar to the early phagosome. Taken together, our findings
56
57 565 shape the view that neutrophils are capable of starving microbial pathogens intra-
58
59 566 and extracellularly from key metal nutrients such as Zn and Fe, remarkably even if
60
567 they release metal containing proteins by bursting open during NETosis. Due to the
568
569 568 detection limitations and their lower abundance, we could not conclusively follow Mn
570
571 569 and Cu. Our data indicates though that void vacuoles are also low in Cu. On these
572
573 570 grounds, it would be worthwhile to investigate whether microbial pathogens target

1
2
3 571 secreted or NET-released metal containing proteins as micro nutrient sources. An
4 572 interplay similar to that of Fe in other settings seems very plausible ⁸.
5
6 573 In addition to Zn, Fe, Cu, and Mn, we also detected a group of metals that are less
7
8 574 renowned for their biological function or mostly described for their toxicity: Co, Ni, Pb,
9
10 575 and Sr. All metals besides Sr were found to be enriched in the nucleus of neutrophils;
11 576 Sr was present at higher concentration in the cytoplasm. Interestingly, Ca, which
12
13 577 behaves very similar to Sr, was enriched in the nucleus, and showed lower
14
15 578 abundance in the cytoplasm. Due to the similarities of Ca and Sr, Sr accumulated in
16 579 the bones of an exposed human. Co is an essential trace element, but also toxic at
17
18 580 high concentrations. It is only found in humans as part of the cofactor cobalamin or
19 581 vitamin B12 (VitB12), which is exclusively produced by commensal bacteria in the
20
21 582 gastro-intestinal tract. Amongst the small number of VitB12-binding proteins in
22
23 583 humans, transcobalamin I was identified in neutrophils ⁴⁸. The protein is localized in
24 584 secondary granules and can be secreted to bind VitB12. Thus, transcobalamin I is
25
26 585 not necessarily saturated with VitB12 in the granules. To our knowledge, no nuclear
27
28 586 cobalamin-containing enzymes have been described, yet. Nevertheless, it was
29
30 587 shown that human keratinocytes for instance accumulate Co in the nucleus and
31 588 perinuclear areas ³². Ni, one of the most toxic of these metals, has no known
32
33 589 biological function in eukaryotes, but is found in a variety of prokaryotic enzymes. Pb
34
35 590 is a known environmental pollutant that accumulates in our bodies in many organs,
36
37 591 most persistently in the bones. Notably, all 4 elements have been detected in whole
38
39 592 blood of healthy individuals that were considered “free of exposure” to any heavy
40
41 593 metal contamination ^{49, 50}. Since the majority of all white blood cells are neutrophils, it
42
43 594 seems reasonable to assume that neutrophils contributed to this detection in whole
44
45 595 blood. As all blood cells are generated in the bone marrow, neutrophils are unlikely
46
47 596 the only blood cells to contain Co, Ni, Pb, and Sr. In conclusion, we have detected Co,
48
49 597 Ni, Sr, and Pb in isolated neutrophils from two individuals living under supposedly
50
51 598 non-exposed conditions. This data indicates an accumulation of Co, Ni, and Pb in the
52
53 599 nucleus, whereas Sr is present in the vicinity of the outer cell membrane in
54
55 600 unstimulated neutrophils.
56
57 601 In the present study, we used two different approaches for SR-XRF with their
58
59 602 respective benefits and disadvantages: Sectioned samples analyzed at nanoscopic
60
603 resolution allowed us to have highly detailed insights into intact neutrophils and
604
605 compare the areal concentration in nucleus and cytoplasm. In contrast, the

1
2
3 605 microscopic approach with whole freeze-dried neutrophils/NETs enabled us to
4 606 quantify the neutrophil metallome and analyze element distributions of neutrophils
5 607 forming NETs (both intermediate and final stages of NETosis). Substantial benefits of
6 608 SR-XRF are 1) the extreme sensitivity, with the potential of single atom detection at
7 609 future nano-beam facilities for transition metals; 2) the minimal sample preparation
8 610 required: cells do not need to be lysed and diluted – factors that might affect the
9 611 reliability - in any other way than the final fixation; 3) the potentially non-destructive
10 612 character: under right measuring conditions samples can be stored and re-analyzed
11 613 at later periods; and 4) the spatial information: individual cells meeting all
12 614 requirements can be selected and analyzed with submicron resolution. Artifacts
13 615 influencing the determined metal distributions are therefore, assuming an appropriate
14 616 sample preparation method and experimental design, rather unlikely. As described,
15 617 we utilized SR-XRF to determine the neutrophil metallome to complement our
16 618 measurement using ICP-MS. Due to the time consuming character of SR-XRF, we
17 619 only analyzed three individual cells, whereas for ICP-MS each sample contained 10^7
18 620 neutrophils. This is, together with the distinct sample preparations, most likely the
19 621 major reason for the deviations between the results of the two different methods.
20 622 Moreover, uncertainties in calibration and interfering background signals are factors
21 623 which might influence Fe concentration measurement using SR-XRF. Quantification
22 624 of Fe by ICP-MS on the contrary, might be hampered by spectral interferences.

23
24
25
26
27
28
29
30
31
32
33
34
35
36
37 625 Nevertheless, the usage of SR-XRF in actual *in vitro* infections or sections from *in*
38 626 *vivo* infection (e.g. as tissue sections) seems very promising. Earlier studies have
39 627 demonstrated, for instance, the cellular reduction of Fe and Zn in *Histoplasma*-
40 628 infected macrophages⁵¹ or the specific enrichment of Cu in the phagolysosome
41 629 containing *Mycobacteria*⁵². These and similar phenomena are ideal candidates for
42 630 SR-XRF analysis at the nanoscale – adding new information about elemental
43 631 distribution and concentrations. Meticulously describing the trace elemental
44 632 composition during different stages of infection within affected organs might even
45 633 identify new targets for antimicrobial therapy. Trace elements are essential for
46 634 microbial growth and their removal could be a potential treatment for infections. The
47 635 lack of certain metals cannot be easily overcome by mutagenesis leading to
48 636 resistance, which makes it a promising target for further research.

49
50
51
52
53
54
55
56
57
58 637
59
60

638

639 **Materials & Methods**

640 *Chemicals and solutions*

641 Unless stated otherwise, chemicals and solutions were purchased from Sigma-
642 Aldrich.

643

644 *Isolation of neutrophils from venous blood*

645 Neutrophils were isolated from human venous blood by using an isolation technique
646 that combines separation on Histopaque-1119 (Sigma-Aldrich) and Percoll (GE
647 Healthcare). Venous blood from human donors was received upon fully informed
648 written consent according to the guidelines of the local ethical committee (Regionala
649 etikprövningsnämnden i Umeå). Briefly, fresh blood was layered in a 1:1 ratio on top
650 of Histopaque-1119, followed by centrifugation at 800 x g for 20 min. The resulting
651 white-blood-cell containing phase was demounted and cells were washed by adding
652 5-6-fold volume of PBS with 0.5 % human serum albumin (HSA). Cells were pelleted
653 by centrifugation for 5 min at 300 x g. The cell pellet was resuspended and applied
654 onto a discontinuous gradient of phosphate-buffered Percoll with the concentrations
655 85 %, 80 %, 75 %, 70 % and 65 %. Cell separation occurred on the gradient during
656 centrifugation at 800 x g for 20 min. Cells accumulated at the interphase between
657 75% and 70% were collected and washed as described before. Finally, cells were
658 taken up in RPMI medium (Lonza).

659 *Neutrophil lysate preparation for ICP-MS*

660 Freshly isolated neutrophils from 8 different healthy donors were lysed. For each
661 sample, 10^7 neutrophils were taken up in 100 μ l HEPES-buffered RPMI and NaOH
662 (99.99 % metals basis, semiconductor grade) was added to reach 0.25 M in 200 μ l.
663 This mixture was incubated for 2 h at 65 °C with vigorous shaking. Subsequently,
664 lysates were sonicated for 1 h in a sonification bath. Samples were stored at -20 °C
665 up to further use. J774 cells (9×10^6) and HeLa cells (5×10^6) were handled
666 accordingly. A biological replicate was therefore either a different blood donor or a
667 different flask and passage of the cultured cells.

668 *NET supernatant preparation for ICP-MS*

1
2
3 669 Neutrophils were diluted in HEPES-buffered RPMI with or without supplementation of
4 670 different concentrations of Zn sulfate (99.999% metals basis). To avoid variations,
5 671 RPMI from only one batch was used for all sample preparations for ICP-MS. Into
6 672 each well of a 24-well plate, 500 μ l cell suspension containing 10^6 cells were seeded
7 673 and then stimulated with 100 nM PMA (Sigma-Aldrich). NET formation occurred
8 674 during a 4 h incubation at 37° C with 5 % CO₂. After this, 400 μ l of the supernatant
9 675 were harvested and cell debris was pelleted by centrifugation for 10 min at 21,000 x
10 676 g. 300 μ l of the supernatant were transferred onto a Vivaspin-500 centrifugal
11 677 column(Sartorius) with a molecular weight cut-off of 3 kDa (corresponding ca. 27
12 678 amino acids). The supernatants were filtered by centrifugation for 30 min at 10,000 x
13 679 g at 4 °C. 200 μ l of the flow through were collected into new reaction tubes and
14 680 stored at -20 °C for further use.

23 681 *ICP-MS measurement*

25 682 The concentrations of trace metals were determined with inductively coupled plasma
26 683 mass spectrometry (ICP-MS, PerkinElmer/Sciex Elan DRC-e instrument) operated in
27 684 reaction cell mode with 0.6 ml/min oxygen and an RPq-value of 0.45. The instrument
28 685 was equipped with a microconcentric PFA nebulizer (Elemental Scientific Inc.)
29 686 combined with a quartz cyclonic spray chamber (Elemental Scientific Inc.) set to 4
30 687 °C. A nebulizer gas flow rate of 0.66 L min⁻¹ and a plasma RF power of 1200 W were
31 688 used. The ⁵⁵Mn, ⁵⁶Fe, ⁵⁷Fe, ⁶³Cu, ⁶⁵Cu, ⁶⁴Zn, ⁶⁶Zn and ⁶⁸Zn isotopes were monitored
32 689 with a dwell time of 50 ms and a total measurement time of 1 min 48 s. The obtained
33 690 isotope distributions were compared with the theoretical patterns to verify the
34 691 absence of spectral interferences. Quantification was done by external calibration
35 692 using indium (monitoring isotope ¹¹⁵In) as internal standard. Sample solutions were
36 693 typically diluted 40 times with Milli-Q water (> 18 M Ω .cm, Milli-Q Advantage A10
37 694 Ultrapure Water Purification System, Merck Millipore) containing 1 % HNO₃ prior to
38 695 analysis.

49 696 *Sample preparation for beamline P06, PETRA III*

51 697 Neutrophils were seeded directly on a 5x5 mm² silicon nitride window (Silson Ltd,
52 698 Northampton, UK, 1.5x1.5 mm² membrane size, 200 nm membrane thickness). 5 *
53 699 10³ cells were added in a 10 μ l drop of HEPES-buffered RPMI and NET formation
54 700 was induced with 100 nM PMA. Incubation occurred as described earlier. After the
55 701 incubation, cells were washed very briefly with ultraclean H₂O and plunge-frozen in
56
57
58
59
60

1
2
3 702 liquid ethane. After 1 h storage in liquid nitrogen, samples were transferred into a
4 703 home-built freeze dryer, based on conventional metal block cooled with liquid
5 704 nitrogen, and samples were lyophilized for 48 h.

6
7
8
9 705 *Experimental set-up beamline P06, PETRA III*

10 706 Measurements were performed at the P06 Hard X-ray Micro/Nanoprobe at PETRA
11 707 III, Hamburg, Germany. The primary beam is generated by a 2 m long spectroscopy
12 708 undulator U32 having 60 periods with 31.4 mm period length and output power of 3.8
13 709 kW. The beam was monochromatized by a Si(111) double crystal monochromator
14 710 having an energy resolution of $1.4 \times 10^{-4} \Delta E/E$, set to a beam energy of 20.5 keV. A
15 711 KB-system (JTEC Corporation, Osaka, Japan) was used to provide a beam size of
16 712 $0.5 \mu\text{m}$ horizontally and $0.4 \mu\text{m}$ vertically at a working distance of 200 mm measured
17 713 from the second mirror, with an estimated flux density of approx. 10^{11} photons/s/ μm^2 .

18
19
20
21
22
23
24
25 714 *Sample preparation for beamline ID22NI, ESRF*

26 715 In a $45 \mu\text{l}$ droplet, 2.5×10^4 neutrophils in HEPES-buffered RPMI were seeded onto a
27 716 1.4 mm sapphire disk (Leica consumables nr. 16706849). NET formation was
28 717 induced by adding 100 nM PMA or cells were left unstimulated. Stimulated cells were
29 718 incubated for up to 4 h at 37°C with 5% CO_2 . Then, the medium was carefully
30 719 removed, cells were washed twice very briefly with a droplet of ultraclean H_2O (to
31 720 avoid osmotic burst) and $50 \mu\text{l}$ of 20% w/V BSA in PBS (Sigma) were added onto each
32 721 sapphire disk as a cryoprotectant. Cells were in contact with the BSA-containing PBS
33 722 only very briefly to minimize this inevitable step affecting the element integrity of the
34 723 cells. The sapphire disc was then very quickly inserted in a membrane carrier (Leica
35 724 consumables nr. 16707898, 1.4 mm diameter, $100 \mu\text{m}$ thickness) and frozen
36 725 immediately in a high-pressure freezer (EM PACT; Leica Microsystems, Vienna,
37 726 Austria). Freeze substitution was carried out using a Leica EM AFS2 (Leica
38 727 Microsystems) in dry acetone with 0.1% glutaraldehyde over 4 days as follows: -90°
39 728 C per hour increase for 15 hours, and -30°C for 24 hours. Samples were then
40 729 washed 3 times in pure acetone and slowly warmed up to 4°C , infiltrated stepwise
41 730 over 3 days at 4°C in Spurr's resin (solution composed of NSA, ERL 4221, DER 736
42 731 and DMAE from emsdiasum.com, Hatfield) and embedded in capsules. The
43 732 polymerization was performed at 70°C for 16h. Ultrathin ($\sim 60 \text{ nm}$) sections intended
44 733 for EM were made using an ultramicrotome (Leica EM UC6) and post-stained in a
45 734 Leica EM AC20 for 40 min in uranyl acetate at 20°C and for 10 min in lead citrate at

1
2
3 735 20°C. Grids were viewed with a JEM 1010 transmission electron microscope (JEOL,
4 736 Tokyo, Japan) operating at 80 kV using Image Plate Technology from Ditabis
5 737 (Pforzheim, Germany). Thin sections (2 μm) were cut and deposited on square
6 738 silicon nitride (Si_3N_4) ultra-thin membranes in square silicon nitride supporting frames
7 739 from Silson Ltd, Northampton, UK (3.0 x 3.0 mm membrane size, 500 nm membrane
8 740 thickness, 7.5 x 7.5 mm frame size and 200 μm frame thickness).

13
14 741 *Experimental set-up beamline ID22NI, ESRF*

15
16 742 The scanning nano-XRF experiments were performed at the ID22NI XRF nanoprobe
17 743 at the European Synchrotron Radiation Facility (ESRF). This instrument was installed
18 744 at a high- β straight section equipped with two different undulators covering an energy
19 745 range of 6-70 keV. The ID22NI nanoprobe (currently replaced by NINA) was
20 746 dedicated to hard X-ray nanoanalysis allowing nano-XRF and absorption/phase
21 747 contrast nanotomography. X-ray focusing was obtained by a crossed elliptical Rh
22 748 coated graded-multilayer mirror-pair in the Kirkpatrick-Baez (KB) geometry. X-rays
23 749 are collected and focused in both vertical and horizontal axis at a glancing angle
24 750 (<3.5 mrad). The first mirror, coated with a graded multilayer plays both the role of
25 751 vertical focusing device and monochromator, resulting in a very high flux (*exceeding*
26 752 10^{11} photons/s) and a medium monochromaticity ($\Delta E/E \approx 10^{-2}$). In our case the beam
27 753 size was determined by knife-edge scans of a Au test pattern and determined to be
28 754 64 nm vertically and 54 nm horizontally at an excitation energy of 17 keV.

38
39 755 *Live cell imaging of Zn pool during NET formation*

40 756 Human neutrophils (5×10^6), stained with 20 μM FluoZin-3 (Life Technologies), were
41 757 seeded into a 35 mm glass bottom micro-well dish (MatTek, Ashland, MA, USA).
42 758 Neutrophils were stimulated with 100 nM PMA and kept at cell-culture conditions
43 759 throughout the entire measurement (5% CO_2 and 37° C). Pictures, phase contrast
44 760 and green fluorescence, were taken using a 60x objective every 2 min for a period of
45 761 2.5 h (beginning at 15 min *post stimulation*) using a Nikon eclipse Ti live-cell
46 762 microscope operated by NIS-Elements AR 3.2. software.

52
53 763 *Quantification of SR-XRF measurements and image segmentation*

54 764 All quantitative results shown were obtained by measuring NIST standard reference
55 765 materials (SRMs). For the ID22NI measurements (ESRF, Grenoble, France), a total
56 766 amount of 17.4 mg powder of NIST SRM 1577c (bovine liver) was pressed into a

1
2
3 767 self-supporting pellet of 13mm diameter resulting in an areal density of 13.11
4 768 mg/cm². The pellet was measured for 1100 s using a raster scan to compensate for
5
6 769 possible inhomogeneities. For the P06 beamline measurements (PETRA III,
7
8 770 Hamburg, Germany), a NIST SRM 613 (trace elements in glass) and a MPI DING
9
10 771 ATHO standard (both prepared as flat samples with a thickness of 100 µm) were
11 772 measured for 1100 seconds using the same measuring strategy described
12
13 773 previously. The obtained spectra were deconvoluted using Analysis of X-ray spectra
14
15 774 using Iterative Least squares AXIL⁵³ to obtain the net line intensities, which were
16 775 then normalised to the incoming photon flux, corrected for detector dead time and for
17
18 776 self absorption effects. Spectral data was then batch processed using an inhouse
19 777 developed software package called MICROXRF2. Manual image segmentation (or
20
21 778 clustering) was performed on the obtained element maps of the unstimulated
22
23 779 neutrophils, indicating nucleus, cytoplasm and cell. The individual point spectra
24
25 780 belonging to a single segment were then summed and net line intensities of the
26
27 781 segment were obtained using AXIL.

28 782 Quantification was based on a fundamental parameter approach which exploits the
29
30 783 theoretical relation between the net-line intensities and the elemental concentrations
31
32 784 (Sherman, 1955). The elemental yields of the elements of interest were calculated
33
34 785 from the measured standard reference material taking into account: 1) variations in
35
36 786 incoming beam intensity (related to varying synchrotron ring current and small
37
38 787 variations in alignment of beamline optical components) by using ionisation chamber
39
40 788 values, 2) the use of absorbers (3000 µm Al in case of NIST SRM 1577c) and 3)
41
42 789 detector dead time (registered for every scanned point).

43 790 The elemental intensity maps were converted into areal concentration distributions
44
45 791 (expressed in µg/cm²) by dividing the pixel values in the normalised elemental maps
46
47 792 (normalised to dead time and storage ring current) by the areal elemental yields. In
48
49 793 order to determine the so-called “relative enrichment factors“ for the relevant
50
51 794 elements in the nucleus versus the cytoplasm, the sum spectra of the nucleus and
52
53 795 the cytoplasm were first normalised to the Compton scattering peak and the ratios of
54
55 796 the relevant elemental intensities were taken.

56 797 *Statistical analysis*

57 798 Unless stated otherwise, all statistical calculations have been performed using
58
59 799 Microsoft Excel. Further statistical analysis was performed using Graphpad Prism
60

1
2
3 800 Software 5. For the quantification of NETs supernatants, data was fitted using a non-
4 801 linear Michaelis-Menten fit.
5
6 802
7
8
9
10
11
12
13
14
15
16
17
18
19
20
21
22
23
24
25
26
27
28
29
30
31
32
33
34
35
36
37
38
39
40
41
42
43
44
45
46
47
48
49
50
51
52
53
54
55
56
57
58
59
60

803

804 **Acknowledgments**

805 We would like to thank Quinten Remijnsen for the help during the neutrophil
806 stimulation experiment (Postdoctoral fellow FWO, VIB Department of Molecular
807 Biomedical Research, Ghent University), Jaime Segura, Gema Martinez-Criado
808 (ID22NI beamline staff, ESRF) and Ulrike Boesenberg (P06, Petra III, DESY) for their
809 excellent technical support during the measurements, Maximilian Popp for support
810 during ICP-MS analyses, Roland Nordfeldt for technical support, and also Lena
811 Meyer and Patrick Engström for providing cultured cells.

812 This work was supported by grants for C.F. Urban from the Swedish Research
813 Council VR-M (2011-2393), the Laboratory for Molecular Medicine Sweden (MIMS),
814 the Medial Faculty Umeå (316-886-10) and the Åke Wiberg Foundation (3772734).
815 M.J. Niemiec acknowledges financial support from the J.C. Kempe Memorial Fund.

816 B. De Samber receives a postdoctoral grant from the Fund for Scientific Research
817 Flanders (FWO Vlaanderen, application number 12B3313N). Both E. Vergucht and J.
818 Garrevoet are funded by PhD grants from the Flemish Institute for the Promotion of
819 Scientific and Technological Research in Industry (IWT, Flanders, Belgium). Financial
820 support by the Fund for Scientific Research Flanders (FWO Vlaanderen, Belgium)
821 contract nr. G.0395.11 & Big Science program G.0C12.13 is acknowledged.

822

823

824 **References**

- 825 1. M. R. Bleackley and R. T. Macgillivray, *Biometals*, 2011, 24, 785-809.
- 826 2. W. E. Winter, L. A. Bazydlo and N. S. Harris, *Lab Med*, 2014, 45, 92-102.
- 827 3. M. Hershinkel, E. Aizenman, G. Andrews and I. Sekler, *Sci Signal*, 2010, 3, mr2.
- 828 4. R. A. Festa and D. J. Thiele, *Curr Biol*, 2011, 21, R877-883.
- 829 5. J. Barber, *Biochemistry (Mosc)*, 2014, 79, 185-196.
- 830 6. K. J. Waldron, J. C. Rutherford, D. Ford and N. J. Robinson, *Nature*, 2009, 460, 823-830.
- 831 7. M. I. Hood and E. P. Skaar, *Nat Rev Microbiol*, 2012, 10, 525-537.
- 832 8. R. Sutak, E. Lesuisse, J. Tachezy and D. R. Richardson, *Trends Microbiol*, 2008, 16, 261-268.
- 833 9. T. E. Kehl-Fie and E. P. Skaar, *Curr Opin Chem Biol*, 2010, 14, 218-224.
- 834 10. Y. Fu, F. M. Chang and D. P. Giedroc, *Acc Chem Res*, 2014, DOI: 10.1021/ar500300n.
- 835 11. D. R. Soll, G. W. Bedell and M. Brummel, *Infect Immun*, 1981, 32, 1139-1147.
- 836 12. D. J. Eide, *Biochim Biophys Acta*, 2006, 1763, 711-722.
- 837 13. L. Decaria, I. Bertini and R. J. Williams, *Metallomics*, 2010, 2, 706-709.
- 838 14. C. Y. Wu, J. Steffen and D. J. Eide, *PLoS One*, 2009, 4, e7061.
- 839 15. G. W. Bedell and D. R. Soll, *Infect Immun*, 1979, 26, 348-354.
- 840 16. E. Kolaczowska and P. Kubes, *Nat Rev Immunol*, 2013, 13, 159-175.
- 841 17. N. Borregaard, *Immunity*, 2010, 33, 657-670.
- 842 18. N. Borregaard, O. E. Sorensen and K. Theilgaard-Monch, *Trends Immunol*, 2007, 28, 340-345.
- 843 19. O. Nusse, *ScientificWorldJournal*, 2011, 11, 2364-2381.
- 844 20. V. Brinkmann, U. Reichard, C. Goosmann, B. Fauler, Y. Uhlemann, D. S. Weiss, Y. Weinrauch and A. Zychlinsky, *Science*, 2004, 303, 1532-1535.
- 845 21. T. A. Fuchs, U. Abed, C. Goosmann, R. Hurwitz, I. Schulze, V. Wahn, Y. Weinrauch, V. Brinkmann and A. Zychlinsky, *The Journal of cell biology*, 2007, 176, 231-241.
- 846 22. C. F. Urban, D. Ermert, M. Schmid, U. Abu-Abed, C. Goosmann, W. Nacken, V. Brinkmann, P. R. Jungblut and A. Zychlinsky, *PLoS pathogens*, 2009, 5, e1000639.
- 847 23. M. Bianchi, M. J. Niemiec, U. Siler, C. F. Urban and J. Reichenbach, *The Journal of allergy and clinical immunology*, 2011, 127, 1243-1252 e1247.
- 848 24. S. M. Damo, T. E. Kehl-Fie, N. Sugitani, M. E. Holt, S. Rathi, W. J. Murphy, Y. Zhang, C. Betz, L. Hench, G. Fritz, E. P. Skaar and W. J. Chazin, *Proc Natl Acad Sci U S A*, 2013, 110, 3841-3846.
- 849 25. B. D. Corbin, E. H. Seeley, A. Raab, J. Feldmann, M. R. Miller, V. J. Torres, K. L. Anderson, B. M. Dattilo, P. M. Dunman, R. Gerads, R. M. Caprioli, W. Nacken, W. J. Chazin and E. P. Skaar, *Science*, 2008, 319, 962-965.
- 850 26. L. Mueller, H. Traub, N. Jakubowski, D. Drescher, V. I. Baranov and J. Kneipp, *Anal Bioanal Chem*, 2014, 406, 6963-6977.
- 851 27. A. Martin-Camean, A. Jos, A. Calleja, F. Gil, A. Iglesias, E. Solano and A. M. Camean, *Talanta*, 2014, 118, 238-244.
- 852 28. E. Bjorn, Y. Nygren, T. T. Nguyen, C. Ericson, M. Nojd and P. Naredi, *Anal Biochem*, 2007, 363, 135-142.
- 853 29. R. Evens, K. A. De Schamphelaere, B. De Samber, G. Silversmit, T. Schoonjans, B. Vekemans, L. Balcaen, F. Vanhaecke, I. Szaloki, K. Rickers, G. Falkenberg, L. Vincze and C. R. Janssen, *Environ Sci Technol*, 2012, 46, 1178-1184.
- 854 30. R. Cesareo and G. Viezzoli, *Phys Med Biol*, 1983, 28, 1209-1218.
- 855 31. S. Bohic, K. Murphy, W. Paulus, P. Cloetens, M. Salome, J. Susini and K. Double, *Anal Chem*, 2008, 80, 9557-9566.
- 856 32. R. Ortega, C. Bresson, A. Fraysse, C. Sandre, G. Deves, C. Gombert, M. Tabarant, P. Bleuuet, H. Sez nec, A. Simionovici, P. Moretto and C. Moulin, *Toxicol Lett*, 2009, 188, 26-32.
- 857 33. R. Ortega, P. Cloetens, G. Deves, A. Carmona and S. Bohic, *PLoS One*, 2007, 2, e925.

- 1
2
3 872 34. T. Leonardo, E. Farhi, A. M. Boisson, J. Vial, P. Cloetens, S. Bohic and C. Rivasseau,
4 873 *Metallomics*, 2014, 6, 316-329.
5 874 35. D. Deruytter, J. Garrevoet, M. B. Vandegheuchte, E. Vergucht, B. De Samber, B. Vekemans, K.
6 875 Appel, G. Falkenberg, K. Delbeke, R. Blust, K. A. De Schamphelaere, L. Vincze and C. R.
7 876 Janssen, *Environ Sci Technol*, 2014, 48, 698-705.
8 877 36. J. Lam, M. Herant, M. Dembo and V. Heinrich, *Biophys J*, 2009, 96, 248-254.
9 878 37. Y. Shi, D. D. Ryu and R. Ballica, *Biotechnol Bioeng*, 1993, 41, 745-754.
10 879 38. A. Hosseinzadeh, P. K. Messer and C. F. Urban, *Front Immunol*, 2012, 3, 391.
11 880 39. H. R. Lopez-Mirabal and J. R. Winther, *Biochim Biophys Acta*, 2008, 1783, 629-640.
12 881 40. W. G. Rice, J. M. Kinkade, Jr. and R. T. Parmley, *Blood*, 1986, 68, 541-555.
13 882 41. H. U. Keller, *J Cell Physiol*, 1990, 145, 465-471.
14 883 42. T. Vogl, N. Leukert, K. Barczyk, K. Strupat and J. Roth, *Biochim Biophys Acta*, 2006, 1763,
15 884 1298-1306.
16 885 43. L. Tapia, M. Suazo, C. Hodar, V. Cambiazo and M. Gonzalez, *Biomaterials*, 2003, 24, 169-174.
17 886 44. G. L. Smith, R. A. Jenkins and J. F. Gough, *J Histochem Cytochem*, 1969, 17, 749-750.
18 887 45. S. J. Klebanoff, *J Leukoc Biol*, 2005, 77, 598-625.
19 888 46. N. A. Maianski, J. Geissler, S. M. Srinivasula, E. S. Alnemri, D. Roos and T. W. Kuijpers, *Cell*
20 889 *Death Differ*, 2004, 11, 143-153.
21 890 47. H. Parker, A. M. Albrett, A. J. Kettle and C. C. Winterbourn, *Journal of leukocyte biology*,
22 891 2012, 91, 369-376.
23 892 48. J. Johnston, J. Bollekens, R. H. Allen and N. Berliner, *J Biol Chem*, 1989, 264, 15754-15757.
24 893 49. F. Gil, A. F. Hernandez, C. Marquez, P. Femia, P. Olmedo, O. Lopez-Guarnido and A. Pla, *Sci*
25 894 *Total Environ*, 2011, 409, 1172-1180.
26 895 50. N. B. Ivanenko, A. A. Ivanenko, N. D. Solovyev, A. E. Zeimal, D. V. Navolotskii and E. J.
27 896 Drobyshev, *Talanta*, 2013, 116, 764-769.
28 897 51. M. S. Winters, Q. Chan, J. A. Caruso and G. S. Deepe, Jr., *J Infect Dis*, 2010, 202, 1136-1145.
29 898 52. D. Wagner, J. Maser, B. Lai, Z. Cai, C. E. Barry, 3rd, K. Honer Zu Bentrup, D. G. Russell and L. E.
30 899 Bermudez, *J Immunol*, 2005, 174, 1491-1500.
31 900 53. B. Vekemans, K. Janssens, L. Vincze, F. Adams and P. Vanespen, *X-Ray Spectrometry*, 1994,
32 901 23, 278-285.
33
34
35
36 902
37
38 903
39
40
41
42
43
44
45
46
47
48
49
50
51
52
53
54
55
56
57
58
59
60

904

Figure 1: Metallome comparison of human neutrophils with J774 and HeLa cells.

Cultured J774 and HeLa cells were alkaline lysed and the resulting lysates were quantified by ICP-MS. The average content was related to the average content of human neutrophils, n = 3, and normalized by cell volume.

Figure 2A: Normalized elemental distributions (P, S, Ca, Zn, Fe, Cu, and Mn) of a single resting human neutrophil obtained at P06 beamline (PETRA III, Hamburg). Freshly isolated neutrophils were seeded on a Si₃N₄ membrane and subsequently freeze-dried. Image size is 81 μm x 78 μm, step size is 300 nm and 4 s dwell time/point. The RGB image represents a colored overlay of the elemental intensities corresponding to Ca (red) – Zn (green) and Fe (blue). An optical image was taken by the beamline microscope (2500x magnification).

Figure 2B: Normalized elemental distributions (P, S, Ca, Zn, Fe, Cu, and Mn) of two activated human neutrophils (2 h stimulation) obtained at P06 beamline. Freshly isolated neutrophils were seeded on a Si₃N₄ membrane, stimulated with PMA for 2 h and subsequently freeze-dried. Image size: 73 μm (hor.) x 97 μm (vert.), step size: 1 μm and 5 s dwell time/point. The RGB image represents a colored overlay of the elemental intensities corresponding to Ca (red) – Zn (green) and Fe (blue). An optical image was taken by the beamline microscope (2500x magnification).

Figure 2C: Normalized elemental distributions (P, S, Ca, Zn, Fe, Cu, and Mn) of human neutrophils (4 h stimulation) obtained at the PETRA III P06 beamline. Freshly isolated neutrophils were seeded on a Si₃N₄ membrane, stimulated with PMA for 4 h and subsequently freeze-dried. Image size: 100 μm x 100 μm, step size: 1 μm and 3 s scanning time/point. The RGB image represents a colored overlay of the elemental intensities corresponding to Ca (red) – Zn (green) and Fe (blue). An optical image was taken by the beamline microscope (2500x magnification).

Figure 3A: Normalized elemental distributions (P, S, Ca, Zn, Fe, Cu, and Mn) of a single resting human neutrophil obtained at ID22NI beamline (ESRF, Grenoble). Freshly isolated neutrophils were high pressure frozen, cryosubstituted in resin, sliced in 2 μm thin sections before deposition onto a Si₃N₄ wafer. Image area is 9 μm (hor.) x 7.4 μm (vert.), step size is 50 nm and 300 ms dwell time/point. The RGB image represents a colored overlay of the elements Ca (red) – Zn (green) and Fe (blue). The additional TEM image (lower right panel) was derived from the same sample and selected by similarity in morphology (10,000x magnification).

Figure 3B: Normalized elemental distributions (P, S, Ca, Zn, Fe, Cu, and Mn) of two activated human neutrophils (1 h stimulation) obtained at ID22NI beamline (ESRF, Grenoble). Freshly isolated neutrophils were stimulated with PMA for 1 h, high pressure frozen, cryosubstituted in resin and sliced in 2 μm thin sections before deposition onto a Si₃N₄ wafer. Image area is 15 μm (hor.) x 11.2 μm (vert.), step size is 50 nm and 400 ms dwell time/point. The RGB image represents a colored overlay of the elemental intensities corresponding to Ca (red) – Zn (green) and Fe (blue). The additional TEM image (lower right panel) was derived from the same sample and selected by similarity in morphology (2500x magnification).

1
2
3 959 **Figure 3C: Normalized elemental distributions (P, S, Ca, Zn, Fe, Cu, and Mn) of**
4 960 **activated human neutrophils (2 h stimulation) obtained at ID22NI beamline (ESRF,**
5 961 **Grenoble).** Freshly isolated neutrophils were stimulated with PMA for 2 h, high pressure
6 962 frozen, cryosubstituted in resin, sliced in 2 μm thin sections before deposition onto a Si_3N_4
7 963 wafer. Image area is 15 μm (hor.) x 15 μm (vert.), step size is 50 nm and 300 ms dwell
8 964 time/point. The RGB image represents a colored overlay of the elemental intensities
9 965 corresponding to Ca (red) – Zn (green) and Fe (blue). The additional TEM image (lower right
10 966 panel) was derived from the same sample and selected by similarity in morphology (2500x
11 967 magnification).
12 968
13 969

14 970 **Figure 3D: Normalized elemental distributions (P, S, Ca, Zn, Fe, Cu, and Mn) of**
15 971 **activated human neutrophils (3 h stimulation) obtained at ID22NI beamline (ESRF,**
16 972 **Grenoble).** Freshly isolated neutrophils were stimulated with PMA for 3 h, high pressure
17 973 frozen, cryosubstituted in resin, sliced in 2 μm thin sections before deposition onto a Si_3N_4
18 974 wafer. Image area is 20 μm (hor.) x 14 μm (vert.), step size is 50 nm and 300 ms dwell
19 975 time/point. The RGB image represents a colored overlay of the elements Ca (red) – Zn
20 976 (green) and Fe (blue). The additional TEM image (lower right panel) was derived from the
21 977 same sample and selected by similarity in morphology (2500x magnification).
22 978
23 979

24 980 **Figure 4: NET-mediated reduction of Zn availability.** NET formation was induced in
25 981 neutrophils with PMA for 4 h in the presence of different Zn^{2+} concentrations. The remaining
26 982 Zn concentration was quantified by ICP-MS. Pooled data from three independent ICP-MS
27 983 experiments including samples from 8 healthy donors is shown.
28 984
29
30
31
32
33
34
35
36
37
38
39
40
41
42
43
44
45
46
47
48
49
50
51
52
53
54
55
56
57
58
59
60

985

986 **Table 1: Total metal content of neutrophils determined by ICP-MS.** Freshly isolated
 987 neutrophils from 8 healthy volunteers were alkaline lyzed and resulting lysates were
 988 quantified by ICP-MS. The average and standard deviation of all 8 biological replicates are
 989 displayed.

Element	Atoms per cell	Intracellular concentration (μM)
Zn	$6.07 \pm 1.29 \times 10^7$	275.31 ± 58.61
Fe	$1.64 \pm 0.33 \times 10^8$	743.91 ± 148.62
Cu	$2.26 \pm 0.69 \times 10^6$	10.24 ± 3.11
Mn	$2.49 \pm 0.69 \times 10^5$	1.13 ± 0.31

990

991

992 **Table 2: Comparison and relation of areal concentrations in neutrophil nucleus and**
 993 **cytoplasm.**

994 Unstimulated neutrophils were analyzed individually by SR-XRF (ID22NI beamline, ESRF)
 995 and the areal concentration was determined and compared between nucleus and cytoplasm
 996 in 2 μm thin slices. Trace-level metal content was determined using a NIST SRM 1577c
 997 standard for quantification. The average and standard deviation of three individual cells are
 998 displayed, as well as the corresponding mass-normalized 'enrichment factor' of the nucleus.

Element	Nucleus ($\mu\text{g}/\text{cm}^2$)	Cytoplasm ($\mu\text{g}/\text{cm}^2$)	Enrichment Factor
P	$8.81 \pm 0.33 \times 10^0$	$1.59 \pm 0.33 \times 10^0$	50.11 ± 27.41
S	$1.62 \pm 0.40 \times 10^0$	$3.02 \pm 0.31 \times 10^0$	0.47 ± 0.09
Ca	$8.80 \pm 0.58 \times 10^{-3}$	$2.90 \pm 0.25 \times 10^{-3}$	2.83 ± 0.26
Zn	$2.28 \pm 0.32 \times 10^{-3}$	$6.84 \pm 2.11 \times 10^{-4}$	3.19 ± 0.78
Fe	$1.14 \pm 0.15 \times 10^{-4}$	$8.83 \pm 0.81 \times 10^{-5}$	1.29 ± 0.18
Cu	$2.59 \pm 0.34 \times 10^{-3}$	$4.04 \pm 0.35 \times 10^{-3}$	0.63 ± 0.10
Mn	$2.40 \pm 0.19 \times 10^{-4}$	$1.00 \pm 0.04 \times 10^{-4}$	3.98 ± 0.10

999

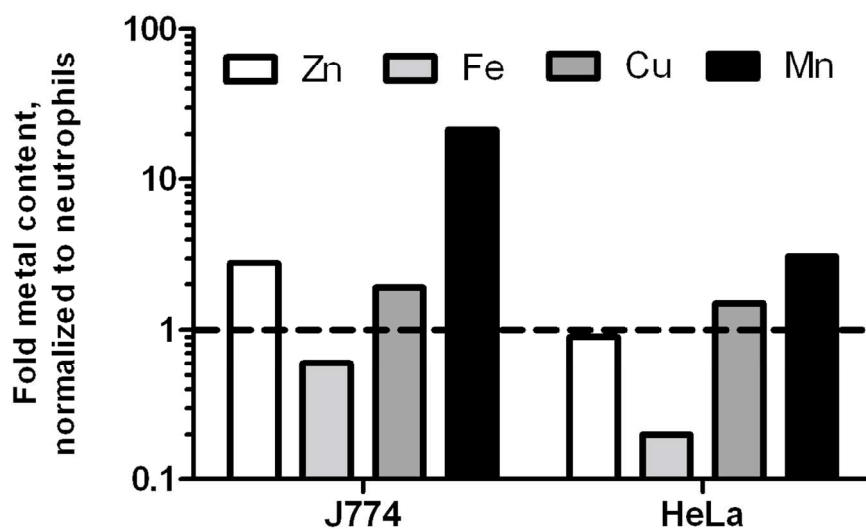


Figure 1: Metallome comparison of human neutrophils with J774 and HeLa cells. Cultured J774 and HeLa cells were alkaline lysed and the resulting lysates were quantified by ICP-MS. The average content was related to the average content of human neutrophils, $n = 3$, and normalized by cell volume.

112x67mm (300 x 300 DPI)

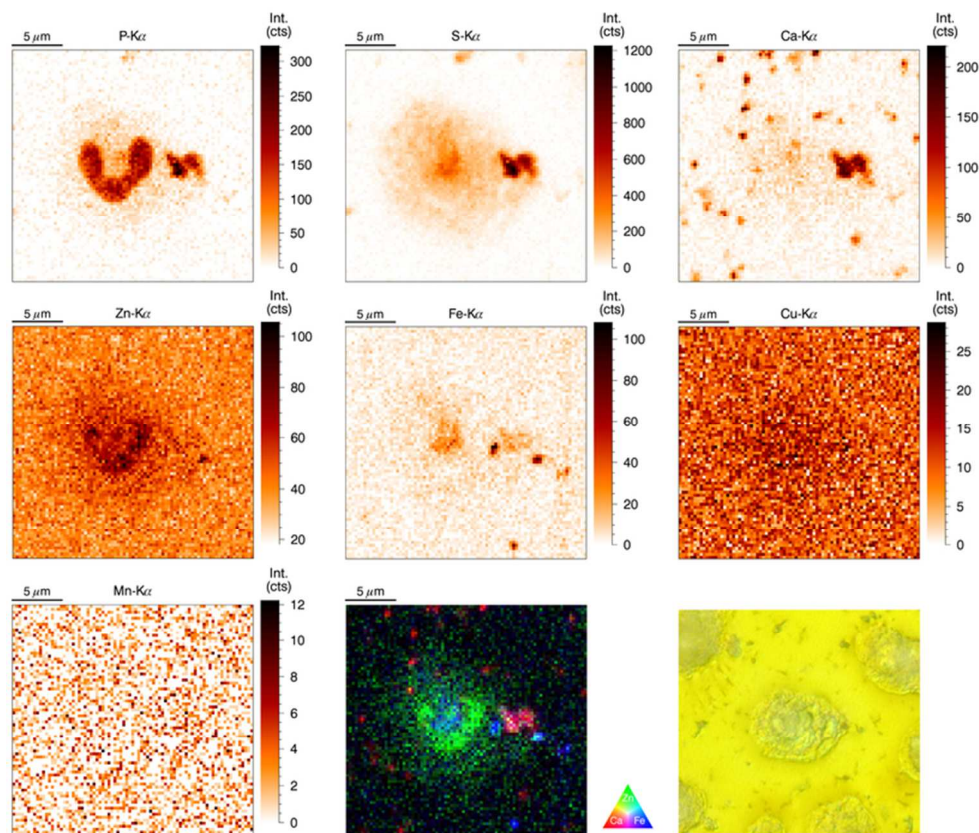


Figure 2A: Normalized elemental distributions (P, S, Ca, Zn, Fe, Cu, and Mn) of a single resting human neutrophil obtained at P06 beamline (PETRA III, Hamburg). Freshly isolated neutrophils were seeded on a Si₃N₄ membrane and subsequently freeze-dried. Image size is 81 μm x 78 μm, step size is 300 nm and 4 s dwell time/point. The RGB image represents a colored overlay of the elemental intensities corresponding to Ca (red) – Zn (green) and Fe (blue). An optical image was taken by the beamline microscope (2500x magnification).
70x58mm (300 x 300 DPI)

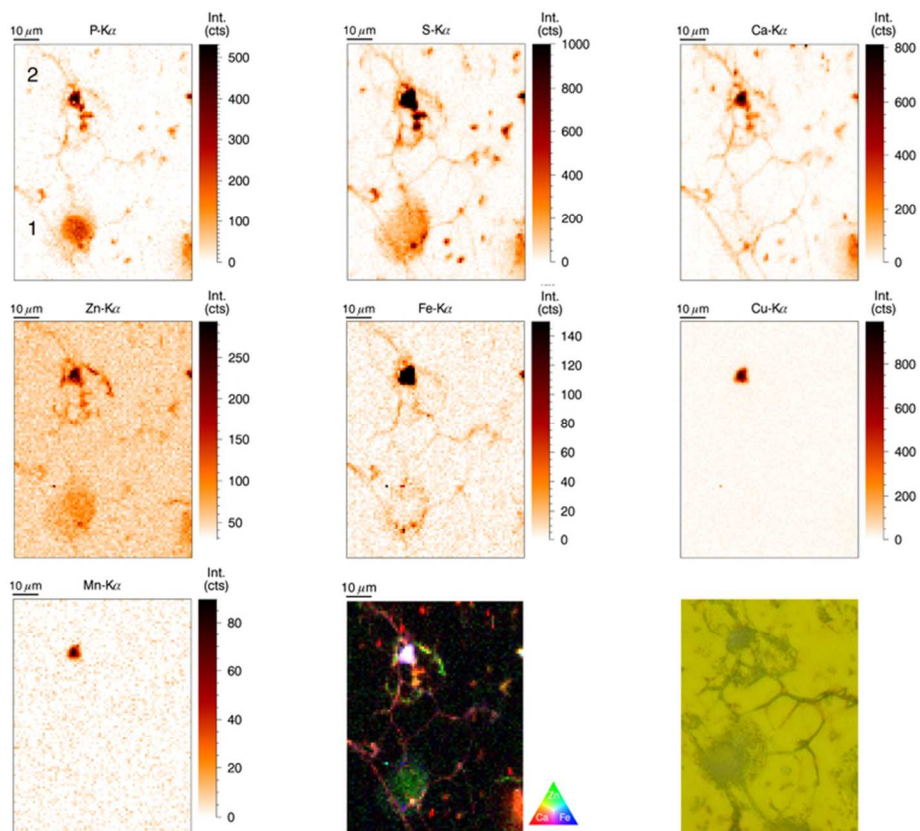


Figure 2B: Normalized elemental distributions (P, S, Ca, Zn, Fe, Cu, and Mn) of two activated human neutrophils (2 h stimulation) obtained at P06 beamline. Freshly isolated neutrophils were seeded on a Si₃N₄ membrane, stimulated with PMA for 2 h and subsequently freeze-dried. Image size: 73 μm (hor.) x 97 μm (vert.), step size: 1 μm and 5 s dwell time/point. The RGB image represents a colored overlay of the elemental intensities corresponding to Ca (red) – Zn (green) and Fe (blue). An optical image was taken by the beamline microscope (2500x magnification).
70x58mm (300 x 300 DPI)

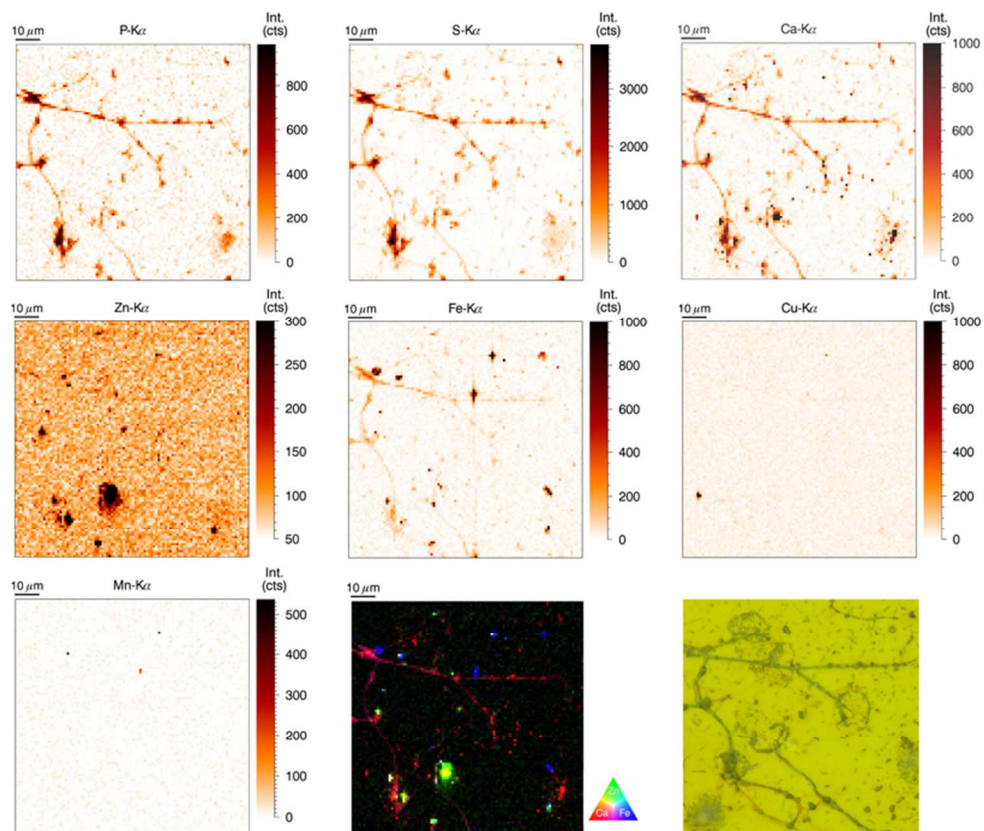


Figure 2C: Normalized elemental distributions (P, S, Ca, Zn, Fe, Cu, and Mn) of human neutrophils (4 h stimulation) obtained at the PETRA III P06 beamline. Freshly isolated neutrophils were seeded on a Si₃N₄ membrane, stimulated with PMA for 4 h and subsequently freeze-dried. Image size: 100 μ m x 100 μ m, step size: 1 μ m and 3 s scanning time/point. The RGB image represents a colored overlay of the elemental intensities corresponding to Ca (red) – Zn (green) and Fe (blue). An optical image was taken by the beamline microscope (2500x magnification).
70x58mm (300 x 300 DPI)

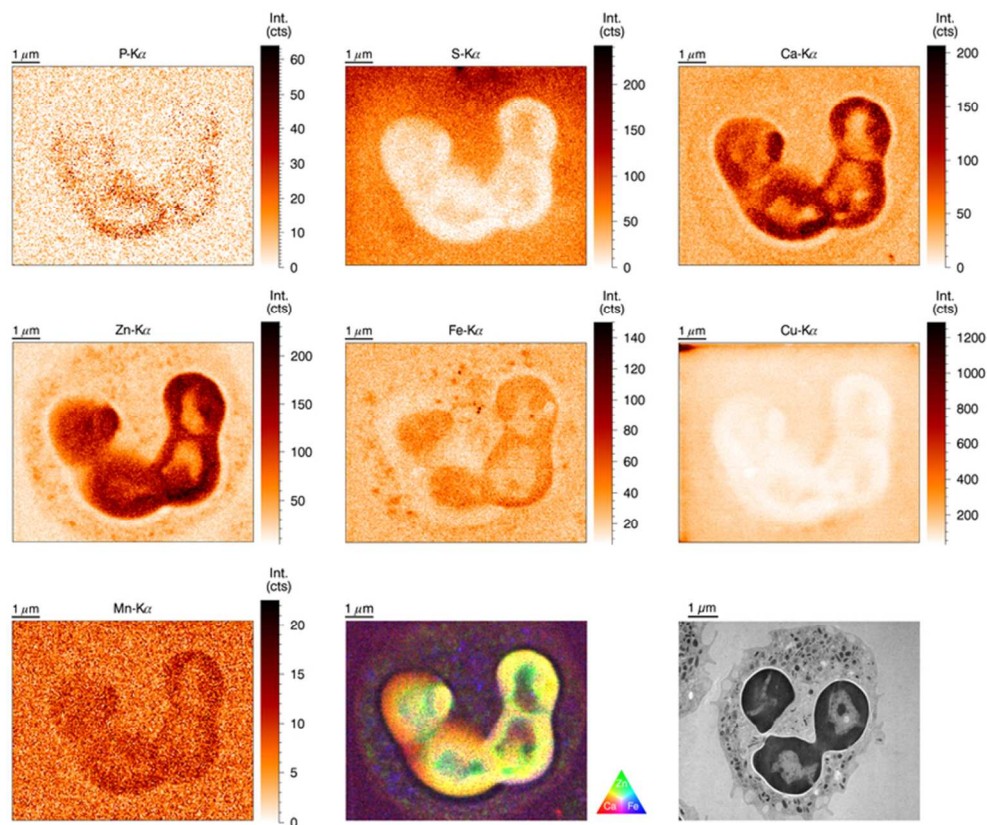


Figure 3A: Normalized elemental distributions (P, S, Ca, Zn, Fe, Cu, and Mn) of a single resting human neutrophil obtained at ID22NI beamline (ESRF, Grenoble). Freshly isolated neutrophils were high pressure frozen, cryosubstituted in resin, sliced in 2 μm thin sections before deposition onto a Si₃N₄ wafer. Image area is 9 μm (hor.) x 7.4 μm (vert.), step size is 50 nm and 300 ms dwell time/point. The RGB image represents a colored overlay of the elements Ca (red) – Zn (green) and Fe (blue). The additional TEM image (lower right panel) was derived from the same sample and selected by similarity in morphology (10,000x magnification).

70x58mm (300 x 300 DPI)

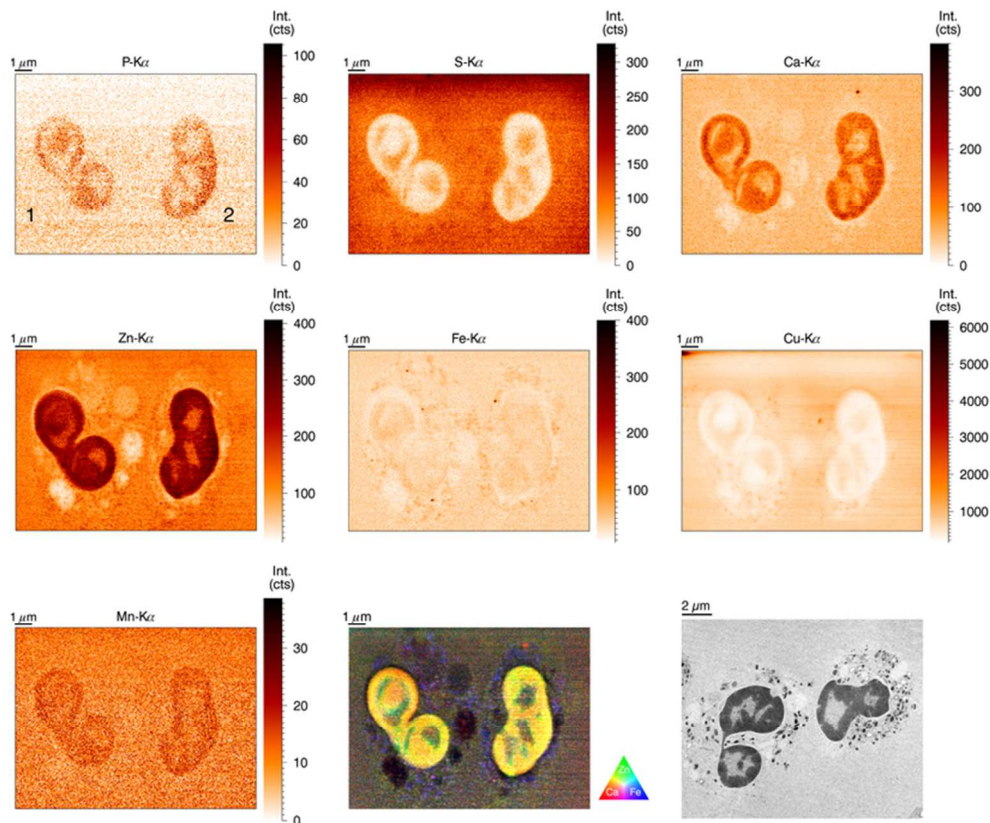


Figure 3B: Normalized elemental distributions (P, S, Ca, Zn, Fe, Cu, and Mn) of two activated human neutrophils (1 h stimulation) obtained at ID22NI beamline (ESRF, Grenoble). Freshly isolated neutrophils were stimulated with PMA for 1 h, high pressure frozen, cryosubstituted in resin and sliced in 2 μ m thin sections before deposition onto a Si₃N₄ wafer. Image area is 15 μ m (hor.) x 11.2 μ m (vert.), step size is 50 nm and 400 ms dwell time/point. The RGB image represents a colored overlay of the elemental intensities corresponding to Ca (red) – Zn (green) and Fe (blue). The additional TEM image (lower right panel) was derived from the same sample and selected by similarity in morphology (2500x magnification). 70x58mm (300 x 300 DPI)

1
2
3
4
5
6
7
8
9
10
11
12
13
14
15
16
17
18
19
20
21
22
23
24
25
26
27
28
29
30
31
32
33
34
35
36
37
38
39
40
41
42
43
44
45
46
47
48
49
50
51
52
53
54
55
56
57
58
59
60

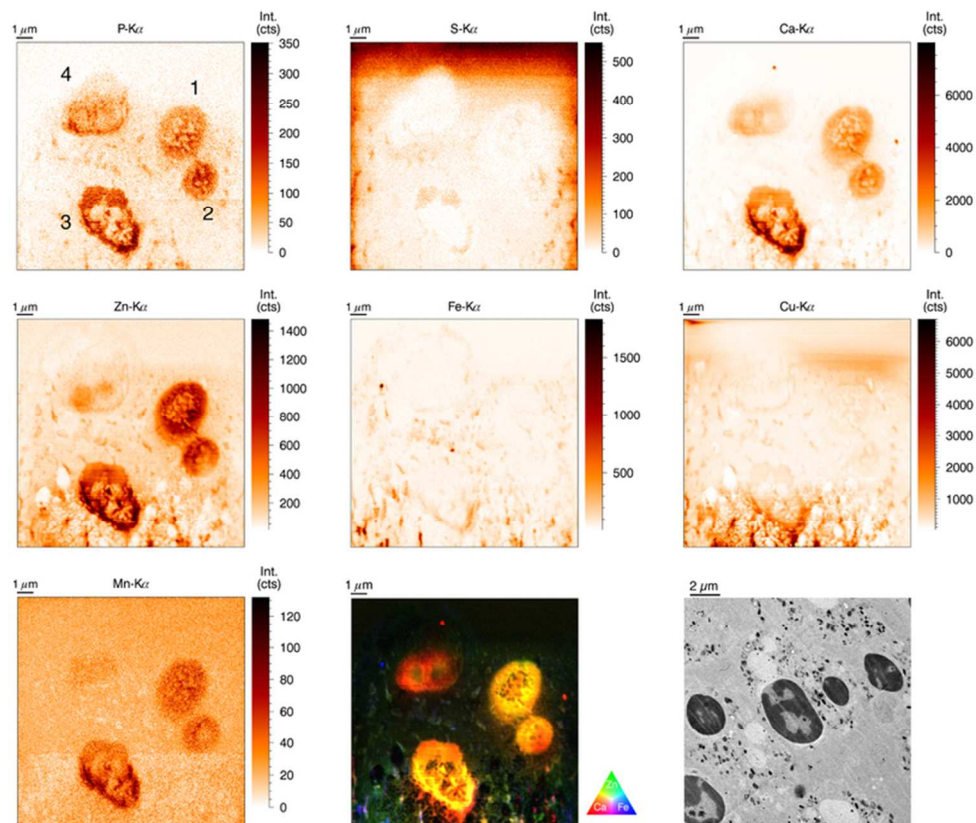


Figure 3C: Normalized elemental distributions (P, S, Ca, Zn, Fe, Cu, and Mn) of activated human neutrophils (2 h stimulation) obtained at ID22NI beamline (ESRF, Grenoble). Freshly isolated neutrophils were stimulated with PMA for 2 h, high pressure frozen, cryosubstituted in resin, sliced in 2 μm thin sections before deposition onto a Si₃N₄ wafer. Image area is 15 μm (hor.) x 15 μm (vert.), step size is 50 nm and 300 ms dwell time/point. The RGB image represents a colored overlay of the elemental intensities corresponding to Ca (red) – Zn (green) and Fe (blue). The additional TEM image (lower right panel) was derived from the same sample and selected by similarity in morphology (2500x magnification). 70x58mm (300 x 300 DPI)

 1
2
3
4
5
6
7
8
9
10
11
12
13
14
15
16
17
18
19
20
21
22
23
24
25
26
27
28
29
30
31
32
33
34
35
36
37
38
39
40
41
42
43
44
45
46
47
48
49
50
51
52
53
54
55
56
57
58
59
60

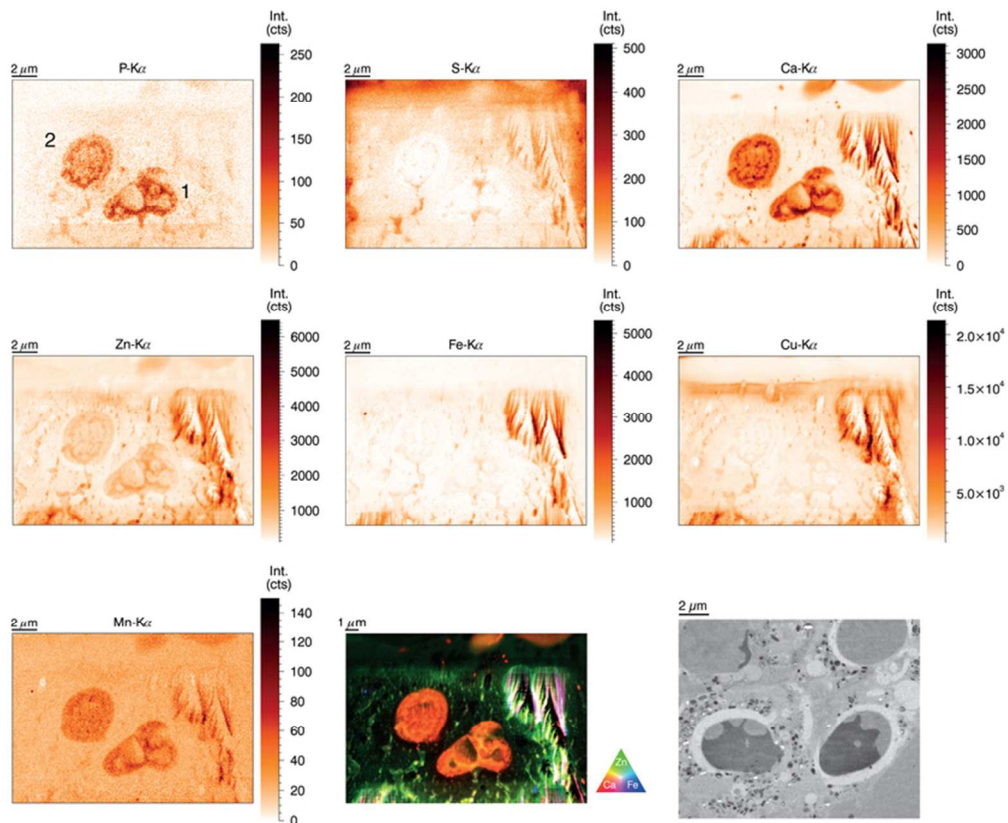


Figure 3D: Normalized elemental distributions (P, S, Ca, Zn, Fe, Cu, and Mn) of activated human neutrophils (3 h stimulation) obtained at ID22NI beamline (ESRF, Grenoble). Freshly isolated neutrophils were stimulated with PMA for 3 h, high pressure frozen, cryosubstituted in resin, sliced in 2 μm thin sections before deposition onto a Si₃N₄ wafer. Image area is 20 μm (hor.) x 14 μm (vert.), step size is 50 nm and 300 ms dwell time/point. The RGB image represents a colored overlay of the elements Ca (red) – Zn (green) and Fe (blue). The additional TEM image (lower right panel) was derived from the same sample and selected by similarity in morphology (2500x magnification).
70x58mm (300 x 300 DPI)

1
2
3
4
5
6
7
8
9
10
11
12
13
14
15
16
17
18
19
20
21
22
23
24
25
26
27
28
29
30
31
32
33
34
35
36
37
38
39
40
41
42
43
44
45
46
47
48
49
50
51
52
53
54
55
56
57
58
59
60

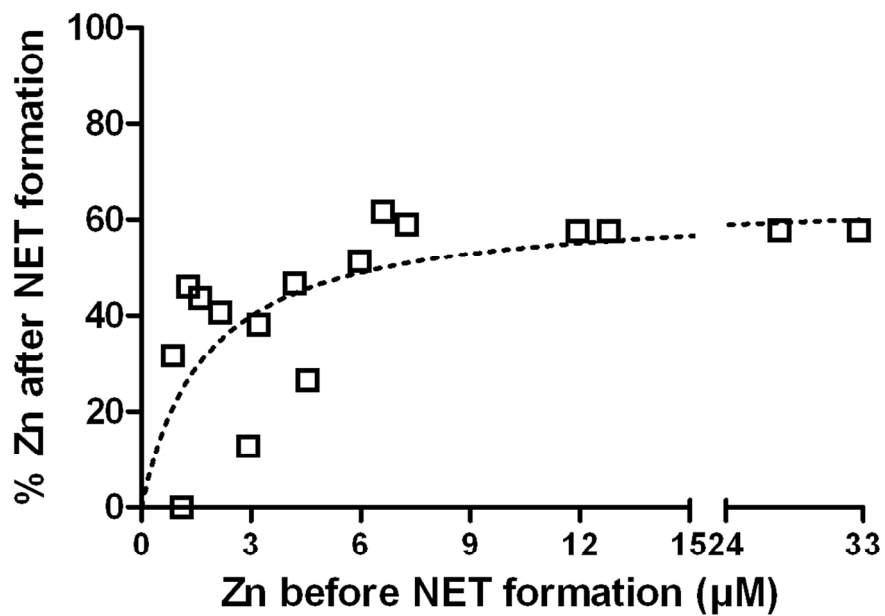


Figure 4: NET-mediated reduction of Zn availability. NET formation was induced in neutrophils with PMA for 4 h in the presence of different Zn²⁺ concentrations. The remaining Zn concentration was quantified by ICP-MS. Pooled data from three independent ICP-MS experiments including samples from 8 healthy donors is shown.

105x73mm (300 x 300 DPI)